Evolution of OH reactivity in low-NO volatile organic compound photooxidation investigated by the fully explicit GECKO-A model

Zhe Peng[1], Julia Lee-Taylor[1,2], Harald Stark[1,3], John J. Orlando[2], Bernard Aumont[4] and Jose L. Jimenez[1]

[1] Department of Chemistry and Cooperative Institute for Research in Environmental Sciences, University of Colorado, Boulder, Colorado 80309, USA

[2] Atmospheric Chemistry Observation and Modeling Laboratory, National Center for Atmospheric Research, Boulder, Colorado 80307, USA

[3] Aerodyne Research Inc., Billerica, Massachusetts 01821, USA

[4] Univ Paris Est Créteil and Université de Paris, CNRS, LISA, F-94010 Créteil, France

Correspondence: Zhe Peng (zhe.peng@colorado.edu) and Jose L. Jimenez (jose.jimenez@colorado.edu)

Abstract. OH reactivity (OHR) is an important control on the oxidative capacity in the atmosphere but remains poorly constrained in many environments, such as remote, rural, and urban atmospheres, as well as laboratory experiment setups under low-NO conditions. ~~OH reactivity (OHR) is an important control on the oxidative capacity in the atmosphere but remains poorly constrained.~~ For an improved understanding of OHR, its evolution during oxidation of volatile organic compounds (VOCs) is a major aspect requiring better quantification. We use the fully explicit Generator of Explicit Chemistry and Kinetics of Organics in the Atmosphere (GECKO-A) model to study the OHR evolution in the low-NO photooxidation of several VOCs, including decane (an alkane), m-xylene (an aromatic), and isoprene (an alkene). Oxidation progressively produces more saturated and functionalized species. Total organic OHR (including precursor and products, OHR_{VOC}) first increases for decane (as functionalization increases OH rate coefficients), and m-xylene (as much more reactive oxygenated alkenes are formed). For isoprene, C=C bond consumption leads to a rapid drop in OHR_{VOC} before significant production of the first main saturated multifunctional product, i.e., isoprene epoxydiol. The saturated multifunctional species in the oxidation of different precursors have similar average OHR_{VOC} per C atom. The latter oxidation follows a similar course for different precursors, involving fragmentation of multifunctional species to eventual oxidation of C1 and C2 fragments to CO_2, leading to a similar evolution of OHR_{VOC} per C atom. An upper limit of the total OH consumption during complete oxidation to CO_2 is roughly 3 per C atom. We also explore the trends in radical recycling ratios. We show that differences in the evolution of OHR_{VOC} between the atmosphere and an environmental chamber, and between the atmosphere and an oxidation flow reactor (OFR) can be substantial, with the former being even larger, but these differences are often smaller than between precursors. The Teflon wall losses of oxygenated VOCs in chambers result in large~~substantial~~ deviations of OHR_{VOC} from atmospheric conditions, especially for the oxidation of larger precursors, where multifunctional species may suffer substantial~~near-complete~~ wall losses, resulting in significant underestimation of OHR_{VOC}. For OFR, the deviations of OHR_{VOC} evolution from the atmospheric case are mainly due to significant OHR contribution from RO_2 and lack of efficient organic photolysis. The former can be avoided by lowering the UV lamp setting in OFR, while the latter is shown to be very difficult to avoid. However, the former may significantly offset the slowdown in fragmentation of multifunctional species due to lack of efficient organic photolysis.

1   Introduction

Photooxidation is a key process altering the concentrations of trace gases in the atmosphere (Levy II, 1971; Atkinson and Arey, 2003). It is also the main contributor to the formation of O_3 and secondary aerosols (Haagen-Smit, 1952; Chameides et al., 1988; Hallquist et al., 2009). Both products are major tropospheric pollutants (Nel, 2005; Cohen et al., 2017) and the latter have large climate impacts (Stocker et al., 2014).

Hydroxyl radical (OH) is the primary oxidizing agent in atmospheric photooxidation (Levy II, 1971). Its atmospheric fate is governed by the species that it reacts with, i.e., OH reactants. The first-order rate constant of OH consumption by an OH reactant is often called its OH reactivity (OHR), equal to the product of the reactant concentration and second-order rate constant with OH. Total OHR (OHR_{tot}), i.e., the sum of OHR across all OH reactants ($OHR_{tot} = \sum_i (k_i * c_i)$), where k_i and c_i are the second-order rate constant with OH and concentration of the ith OH reactant), is the real first-order loss rate constant of OH.

OHR has been measured for over 20 years (Kovacs and Brune, 2001) in various settings, e.g., urban areas (Lu et al., 2013; Whalley et al., 2016), forested areas (Nölscher et al., 2016; Zannoni et al., 2016), and environmental chambers (Fuchs et al., 2013; Nölscher et al., 2014; Fuchs et al., 2017; Novelli et al., 2018)(Nehr et al., 2014; Nölscher et al., 2014). Despite numerous measurements and remarkable technical developments (Yang et al., 2016; Fuchs et al., 2017), a sizable fraction of total OHR in most measurements has not been chemically speciated, leading to so-called "missing reactivity" (Williams and Brune, 2015; Yang et al., 2016). Multiple studies (Nölscher et al., 2016; Whalley et al., 2016; Sato et al., 2017) have attributed missing reactivity to the highly complex mixture of intermediates and products of volatile organic compound (VOC) oxidation, most of which are oxygenated VOCs (OVOCs). Primary VOCs themselves have been found to be the largest contributor of the speciated OHR in many studies (Yang et al., 2016). In order to well understand ambient OHR, the evolution of OHR (including that from OVOCs) during primary VOC photooxidation thus needs to be investigated.

Experimentally, this can be done in environmental chambers. However, only a few such experiments have been published (Nakashima et al., 2012; Nehr et al., 2014; Nölscher et al., 2014; Sato et al., 2017), all under high-NO conditions, where the key organic radical intermediate in VOC oxidation, i.e., organic peroxy radical (RO_2), mainly reacts with NO. To our knowledge, no experiment of this type at low NO, where RO2 can substantially react with hydroperoxy radical (HO2), has been published so far, potentially partially due to the difficulty in experimentally ensuring that low-NO conditions are achieved in chambers (Nguyen et al., 2014). To our knowledge, no experiment of this type at low NO, where RO₂ can substantially react with hydroperoxy radical (HO₂), has been published so far, probably due to the high difficulty in achieving low-NO conditions in chambers. Also, many OVOCs, which may account for missing reactivity, have sufficiently low volatility to significantly partition to chamber walls (Matsunaga and Ziemann, 2010; Krechmer et al., 2016), further complicating these experiments. The OVOC wall losses also often limit operation times of chamber experiments to a few hours, after which the wall losses are so large that meaningful interpretation of experimental results would be difficult.

81   Therefore, the highest equivalent photochemical age that can be reached in chamber experiments is
82   also typically hours and far shorter than would be needed to explore the OHR evolution in later stages
83   of VOC oxidation.

84   Oxidation flow reactors (OFR) are an alternative to chambers with much smaller volume, shorter
85   residence time (and thus smaller wall losses of trace gases), and stronger oxidative capacity (Kang et
86   al., 2007; Brune, 2019; Peng and Jimenez, 2020). The most common version of OFR is equipped with
87   low-pressure Hg lamps emitting UV at 185 and 254 nm, which photolyzes water vapor, O_2, and O_3, and
88   generates a large amount of OH both directly and through subsequent radical reactions. High OH
89   concentration in OFR often leads to equivalent photochemical age of days to weeks (Li et al., 2015;
90   Peng et al., 2015). In principle, OFR can also be employed to explore OHR evolution in VOC oxidation.
91   However, OHR from VOC (OHR_{VOC}, from both precursor and oxidation intermediates/products, in which
92   we include CO as an "organic" product of VOC oxidation) can have strong impacts on oxidative capacity
93   (particularly OH concentration) and hence radical chemistry in OFR at both low (Li et al., 2015; Peng et
94   al., 2015) and high NO (Peng and Jimenez, 2017; Peng et al., 2018). Peng and Jimenez (2020) have called
95   for highly chemically detailed modeling of gas-phase organic chemistry in OFR to assess the impacts of
96   organic OH reactants on OH in a more quantitative manner.

97   In this study, we explore for the first time the OHR evolution in entire low-NO VOC photooxidation
98   processes by modeling. Since chemical mechanism incompleteness causes other models to
99   unsatisfactorily simulate measured OHR_{tot} (Williams and Brune, 2015), we use the fully chemically
100   explicit model GECKO-A (Generator of Explicit Chemistry and Kinetics of Organics in the Atmosphere)
101   (Aumont et al., 2005). We simulate the photooxidation of different types of VOCs in the atmosphere,
102   in chamber, and in OFR, to find out general trends of OHR evolution in VOC oxidation and whether VOC
103   oxidation chemistries in chamber and OFR are representative of that in the atmosphere in terms of
104   OHR evolution.

105   **2   Methods**

106   Here we first discuss the VOC precursor types and conditions selected for the model cases in this
107   study. Then we describe the GECKO-A model and present our additional mechanism, model, and
108   software development required for this study.

109   **2.1   Model cases**

110   The photooxidation of an alkane (decane), an alkene (isoprene), and an aromatic (m-xylene) is
111   investigated under a variety of conditions without any NO. In pristine regions such as open oceans, NO
112   has typical concentrations on the order of 1 ppt (Wofsy et al., 2021) and hence contribute only a few
113   percent to RO_2 loss (Peng et al., 2019). For simplicity, we choose not to maintain such a low NO level in
114   the simulations, but to model zero-NO cases instead. The model cases are listed in Table 1: i) two cases
115   under ambient conditions, one with constant sunlight at solar zenith angle of 45° and the other with
116   diurnally-varying solar radiation and a noontime solar zenith angle of 0°; ii) six cases under typical
117   chamber conditions, i.e., low (10 s-1) / high (100 s-1) precursor OHR without gas-particle-wall
118   partitioning, with gas-particle partitioning (no wall), and with gas-particle-wall partitioning; and iii) five

3

119 cases under OFR conditions, of which two conditions resulting in significant non-tropospheric organic

120 photolysis (Peng et al., 2016) and one leading to remarkable deviations of RO2 fate from that in the

121 troposphere are not recommended in practice, but are still included for completeness since they are

122 similar to conditions in some literature studies (Table 1).~~The model cases are listed in Table 1: i) two~~

123 ~~cases under ambient conditions, one with constant sunlight at solar zenith angle of 45° and the other~~

124 ~~with diurnally-varying solar radiation and a noontime solar zenith angle of 0°; ii) four cases under typical~~

125 ~~chamber conditions, i.e., low (10 s^{-1}) / high (100 s^{-1}) precursor OHR with / without gas-particle-wall~~

126 ~~partitioning; and iii) five cases under OFR conditions, of which two conditions resulting in significant~~

127 ~~non-tropospheric organic photolysis (Peng et al., 2016) and one leading to remarkable deviations of~~

128 ~~RO$_2$ fate from that in the troposphere are not recommended in practice, but are still included for~~

129 ~~completeness since they are similar to conditions in some literature studies (Table 1).~~ For the UV source

130 in chamber cases, we adopt the spectrum of the blacklight and fluorescence light array in the University

131 of Colorado Environmental Chamber Facility (CU Chamber; Krechmer et al., 2017). The CU Chamber has

132 a volume of ~20 m3, a surface area of ~65 m2, and an estimated wall condensation timescales of ~1000

133 s (Krechmer et al., 2016). The parameterization for the reversible gas-wall partitioning is taken from

134 Krechmer et al. (2016) with updates of Liu et al. (2019). Wall partitioning in chambers at equilibrium is

135 a function of the surface-to-volume ratio (Krechmer et al., 2016). The timescale to approach equilibrium

136 is expected to be larger in larger chambers, but still far shorter than the long experiments needed to

137 investigate high photochemical ages. Therefore differences in wall partitioning timescale are not

138 important for this study. Figure S9 of Krechmer et al. (2016) compared the CU Chamber and a few other

139 well-known chambers (including very large ones such as EUPHORE (Siese et al., 2001) and SAPHIR

140 (Rohrer et al., 2005)), showing relatively small differences (within a factor of ~2 in terms of surface-to-

141 volume ratio). Therefore the conclusions about wall partitioning in this study should be approximately

142 applicable to most chambers. The cases under ambient conditions, and chamber conditions with low /

143 high precursor OHR are simulated for 10, and 6 / 30 d, respectively, to encompass an equivalent

144 photochemical age of >10 d in each case (given a typical average ambient OH concentration of 1.5×10^6

145 molecules cm^{-3} in the real atmosphere (Mao et al., 2009); see Fig. 1 for the correspondence between

146 equivalent photochemical age and OH exposure (OH$_{exp}$, i.e., the integral of OH concentration over

147 time)). The simulated OFR in the present work employs the light source parametrization obtained by Li

148 et al. (2015) and Peng et al. (2015). UV at both 185 and 254 nm is used to generate OH, i.e., the

149 "OFR185" mode of operation. The residence time in the OFR is always 3 min. Wall losses in the OFR

150 should be smaller than in the chamber, due to reduced wall contact (Brune 2019), and are not simulated

151 here. As several key parameters of the chamber and OFR cases were obtained experimentally at room

152 temperature and atmospheric pressure in Boulder, Colorado, USA (typically 295 K and 835 mbar), for

153 an easier comparison, we use these values for the temperature and atmospheric pressure of all model

154 cases.

155   In addition, we simulate illustrative cases of methane oxidation, under ambient and OFR

156 conditions (Table 1 and Section 3.1). Note that these two simulations are performed using the GECKO-

157 A generated mechanism (see Section 2.2) in KinSim (Peng and Jimenez, 2019), a chemical-kinetics solver

158 that is not GECKO-A's default, to avoid possible numerical issues in the GECKO-A internal solver, as

159 methane oxidation by OH is very slow (Atkinson and Arey, 2003) and very long runs are needed. ~~Note~~

160 ~~that these two simulations are performed using the GECKO-A generated mechanism (see Section 2.2)~~

161 ~~in another chemical-kinetics solver, KinSim (Peng and Jimenez, 2019), to avoid possible numerical~~

162 ~~issues, as methane oxidation by OH is very slow (Atkinson and Arey, 2003) and very long runs are~~

163 ~~needed.~~ To characterize trends of OHR evolution (see Section 3.5), the ambient cases with constant

164 sunlight are simulated for two more alkanes, i.e., butane and heptane (Table 1). To explore the effects

165 of UV sources in OFR (see Section 3.4), two simulations under a typical OFR condition with an additional

166 broad-spectrum UV source (5 and 10000 times the chamber UV source in this study, respectively) are

167 performed for isoprene (Table 1).

168 **2.2   The GECKO-A model**

169 GECKO-A (Aumont et al., 2005; with updates as described by Camredon et al., 2007; Valorso et

170 al., 2011; Lee-Taylor et al., 2015), is an explicit chemical model which uses known mechanisms and rates

171 supplemented with experimentally-based structure-activity relationships to generate comprehensive

172 atmospheric oxidation mechanisms for organic species. ~~GECKO-A (Aumont et al., 2005; Camredon et al.,~~

173 ~~2007; Valorso et al., 2011), is an explicit chemical model which uses known mechanisms and rates~~

174 ~~supplemented with experimentally-based structure-activity relationships to generate comprehensive~~

175 ~~atmospheric oxidation mechanisms for organic species.~~ The mechanisms are implemented within a box

176 model with a two-step solver (Verwer, 1994; Verwer et al., 1996). In mechanism generation, isomer

177 lumping for mechanism reduction purposes is applied to certain products with branching ratios < 1%

178 (here typically N-containing products, which are not relevant for our simulations). It has a negligible

179 impact on the results.

180 ~~The core isoprene scheme in GECKO-A is adopted from Master Chemical Mechanism v3.3.1~~

181 ~~(Jenkin et al., 2015), while the meta-xylene oxidation mechanism follows MCM v3.2 (Jenkin et al, 2003,~~

182 ~~Bloss et al, 2005) until ring-breaking occurs, whereupon the GECKO-A mechanism generator~~

183 ~~implements the standard SAR protocols.~~ The core isoprene scheme in GECKO-A is adopted from the

184 Master Chemical Mechanism v3.3.1 (Jenkin et al., 2015), while the meta-xylene oxidation mechanism

185 follows MCM v3.2 (Jenkin et al, 2003, Bloss et al, 2005), typically until ring-breaking occurs, whereupon

186 the GECKO-A mechanism generator implements the standard SAR protocols as described by Aumont et

187 al. (2005), Camredon et al. (2007), and Lee-Taylor et al. (2015). Under the zero-NO conditions employed

188 in this study, we find that, in two of the four m-xylene reaction channels (xylenol, 17%; and MXYLO2,

189 4%), some product species persist anomalously owing to lack of alternative reaction pathways in the

190 MCM. We therefore allow GECKO-A to apply the standard SARs to two cyclic non-aromatic products of

191 xylenol (MXYOLO2 and MXYOLOOH in the 51% xylenol OH-oxidation channel, see Scheme S1). We also

192 introduce OH-oxidation of MXYCATECH and MXY1OOH (in the 42% and 7% xylenol OH-oxidation

193 channels), and of MXYLOOH and MXYLAL (in the MXYLO2 channel), assuming similarity to the MCM OH-

194 oxidation of xylenol to MXYOLO2, and with net OH rate constants estimated using the EPA EPISuite

We tested the effect of solver integration timestep length on output precision. The output species concentrations in all simulations but for isoprene OFR (Table 1) converge well as integration timestep decreases (Fig. S1). In the isoprene OFR test cases, the output values oscillate over a small range (<~5%) for integration timesteps ≤ 0.01 s (Fig. S1). Since this numerical error is smaller than typical rate constant measurement uncertainties (from ~10% to a factor of 2–3; Burkholder et al., 2015), let alone the uncertainties related to the SARs used in GECKO-A, it is deemed acceptable for the relevant simulations in this study. The integration timestep for each simulation in the present work is reported in Table 1.

We allow mechanism generation to proceed through to CO_2 production in most cases in this study. The only exception is for extremely low-volatility species (saturation vapor pressure < 10^{-13} atm) which are considered to be completely and irreversibly partitioned to the particle phase. Particle- and wall-phase species are no longer considered in the OHR budget, since heterogeneous oxidation is much slower than gas-phase oxidation (e.g., George and Abbatt, 2010). Gas-particle-wall partitioning is activated only for the chamber cases where wall effects are considered. For the ambient cases and the chamber cases without gas-wall partitioning, gas-particle partitioning is also disabled to avoid artificial condensation of gases into the particle phase. In environments with very low NO (e.g., remote atmosphere), organic aerosol concentration is typically 0.2 µg m^{-3} (Hodzic et al., 2020) while most major intermediates/products have higher saturation concentrations (C*) and hence largely stay in the gas phase. C* is calculated using the parameterization of Nannoolal et al. (2008) (default option of GECKO-A). Although SIMPOL (Pankow and Asher, 2008) was recommended by Krechmer et al. (2016) to estimate C* for the chamber wall partitioning treatment using their parameterization, the C* estimates by the Nannoolal and SIMPOL parameterizations are close (generally within a factor of 2) for the species that can reversibly partition between the gas and wall phases (C* ~ 0.1–1000 µg m^{-3}) in this study. This difference is smaller than the uncertainties of the Krechmer et al. (2016) parameterization. Therefore, the use of the parameterization of Nannoolal et al. (2008) for C* estimation is acceptable.

Concerns have previously been expressed about non-conservation of carbon in GECKO-A (Mouchel-Vallon et al., 2020). This has proven in the current simulations to be almost entirely due to lack of accounting for product CO_2 in some handwritten reactions. We edited the handwritten isoprene and m-xylene schemes (see above and Section 2.2.3) for carbon balance, which reduced simulation-end carbon losses in the m-xylene and isoprene ambient cases with constant UV from 4% and 9%, respectively, to negligible levels (<0.4%; Fig. S2).

For the current study, we have made several updates to GECKO-A, i.e., i) inclusion of key OFR-

specific radical reactions, ii) extension of the UV range considered to cover 185 and 254 nm, and iii) updates to the low-NO m-xylene oxidation mechanism, so that GECKO-A is able to simulate OFR chemistry and the entire process of low-NO m-xylene photooxidation (until CO/CO_2). We will describe these three updates below.

2.2.1 Key radical reactions in oxidation flow reactor

We have added several reactions that are unimportant in the troposphere, but that are required to fully represent the radical chemistry within the OFR (Li et al., 2015). The most important inorganic reactions are $H_2O + hv$ (185 nm) $\rightarrow$ H + OH, $O_2 + hv$ (185 nm) $\rightarrow$ $2O(^3P)$, and $O_3 + hv$ (254 nm) $\rightarrow$ $O(^1D)$ + O_2. These three reactions, together with $O(^3P) + O_2 + M \rightarrow O_3 + M$ and $O(^1D) + H_2O \rightarrow 2OH$, which are already in the GECKO-A inorganic radical chemistry scheme, are responsible for the OH generation in OFR. The OFR radical chemistry has previously been modeled in detail using KinSim (Peng and Jimenez, 2019), which was validated against experimental observations (Li et al., 2015; Peng et al., 2015). A comparison between KinSim and GECKO-A for a range of OFR conditions shows typical agreement between the two models within 2% for key outputs.

Due to high OH in OFR, reaction of RO_2 with OH is also included in mechanism generation, with an assumed rate constant of 1×10^{10} cm^3 $molecule^{-1}$ s^{-1} (Peng et al., 2019). The products of this type of reaction are assumed to be RO (alkoxy radical) + HO_2 for alkyl RO_2 and R (alkyl radical) + CO_2 + HO_2 for acyl RO_2. Although these reactions for certain RO_2 may have reaction intermediates, the reactions of the intermediates (with OH) are believed to be very fast ~~under~~in OFR conditions where OH is much higher than in the atmosphere (Peng and Jimenez, 2020) and hence only the probable final products (no intermediates) of these reactions are included in mechanism generation. The reaction of RO_2 with OH is not included in the mechanisms for the ambient and chamber simulations due to low contribution of this pathway to the RO_2 fate in those cases.

2.2.2 Organic photolysis at 185 and 254 nm

Organic photolysis is assessed in GECKO-A via a lookup table of j-values for reference chromophores pre-calculated at different solar zenith angles with the TUV 1-D radiative transfer model (Madronich and Flocke, 1999). The reference cross-sections used in the model generally do not cover the UV wavelengths at which OFR operates (with narrow peaks at 185 nm and 254 nm) since they are not tropospherically relevant. Thus it was necessary to extend to 185 nm the relevant reference absorption cross-sections. We have done this using literature values via the Mainz UV-Vis spectral atlas (Keller-Rudek et al., 2020) or by extrapolating the available cross-section data, using other similar chromophores as references. Details of all cross-section extensions are given in Table S1. Where quantum yield information was not available, we assume values of unity since photons at 185 and 254 nm are usually sufficiently energetic to make photolysis occur (Ausloos and Lias, 1971). In case of multiple product channels for a photolyzed molecule, the branching ratios of those channels at 185 and 254 nm are estimated through extrapolation of branching ratio data from available ranges followed by a renormalization. Finally, we apply the OFR UV spectrum within TUV to calculate OFR-relevant j-value lookup tables.

2.2.3 Mechanism of low-NO m-xylene oxidation

The meta-xylene oxidation mechanism in GECKO-A follows MCM v3.2 until all aromatic, epoxy, or bridged-peroxy rings are broken (See Scheme S1). Since the MCM was designed for typical urban environments with abundant NO_x, it omits some reaction pathways for other oxidants, assuming them to be of negligible importance. The relevant photolysis loss pathways are slow under ambient conditions and inactive in the OFR case. This leads to persistence and accumulation of certain hydroperoxides and their interconverting peroxy radicals under low-NO conditions. We added two low-NO oxidation reactions to the xylenol branch of the meta-xylene oxidation scheme, Scheme S1. In the 51% branch, we allow the unsaturated bicyclic peroxide "MXYLOOH" to react with, sequentially, OH (estimating k_{VOC+OH} ~ $3e^{-11}$ cm^3 molecule^{-1} s^{-1}) and HO_2 (estimating $k_{RO2+HO2}$ ~ $1e^{-11}$ cm^3 molecule^{-1} s^{-1}), to produce a saturated bicyclic peroxide (denoted "TT8001" in Scheme S1). In the 42% branch, we add a competing O_3 reaction with the alkoxy radical "MXCATEC1O", producing an unsaturated carbonyl alkoxy radical "1T8000" which eliminates CH3 to form the unsaturated cyclic hydroxy dicarbonyl "TU7000". Both products are then further oxidised via the standard GECKO SARs.

2.3 GECKO Loader and Plotter

To allow GECKO-A outputs, which are usually highly complex and voluminous, to be explored and visualized in detail on standard (non-UNIX) personal computers, we have developed the GECKO Loader and Plotter based in the data-analyzing and graphic-making package Igor Pro 8.0 (WaveMetrics, Lake Oswego, Oregon, USA). This tool assists on the rapid and detailed analysis of model-chamber/OFR comparison studies.

Specifically, the GECKO Loader and Plotter facilitates: i) filtering the (sometimes extremely large and finely-resolved) model results time series to examine specific characteristics, ii) identifying the most abundant and/or influential species in each phase (gas, particle, and wall), iii) selecting species by specific chemical identity (molecular formula, specific formula, and/or functional group identity), iv) plotting time series of individual species and their formation/destruction rates, v) assessing and displaying aggregated properties (volatility distribution, mass spectrum, Henry's law constant distribution) of the product mixture and subsets thereof, and vi) calculating bulk characteristics of the simulation (OH_{exp}, OHR_{VOC}, light intensity, elemental ratios etc.) and relating species abundances to them.

3 Results and discussions

In this section, we will show the evolution of OHR_{VOC} in the photooxidation of different precursors under various conditions. To aid the presentation of this evolution for larger precursors, whose oxidation is more complex, the oxidation of the simplest VOC, i.e., methane, will be first discussed. After presenting the results of individual precursors, we will compare the results between conditions and between precursors to illustrate the general trends. Along with the OHR evolution, OH recycling ratio (β_1, defined as number of OH molecules generated from organic reactions per OH consumed by organics) and HO_x (= OH + HO_2) recycling ratio (β_2, defined as number of OH and HO_2 molecules generated from organic reactions per OH consumed by organics) will also be discussed, as they are

309 important parameters that may considerably affect the budget of atmospheric oxidizing agents (Stone

310 et al., 2012) and the HO_2-to-OH ratio and RO_2 chemistry in OFR (Peng et al., 2015, 2019).

3.1 Methane

312   To explain one of the main features in the OHR evolution in VOC photooxidation, i.e., OHR_{VOC}

313 peaking at a certain OH_{exp}, the oxidation of CH_4 is employed as an example because of its simpler

314 mechanism (Scheme S2). The results of this oxidation under the ambient condition show that OHR_{VOC}

315 peaks at an OH_{exp} of about 1×10^{13} molecules cm^{-3} s (Fig. S3). As the OHR of the precursor always

316 decreases during its oxidation, the appearance of such a peak of OHR_{VOC} before all VOCs are finally

317 oxidized to CO_2 indicates that the OHR increase from intermediates and products is faster than the OHR

318 decrease of the precursor. This is obviously the case for CH_4 oxidation, as there is no significant CH_4 loss

319 before $OH_{exp} \sim 10^{13}$ molecules cm^{-3} s by its very slow reaction with OH (rate constant on the order of

320 10^{-15} cm^3 $molecule^{-1}$ s^{-1}; Atkinson and Arey, 2003) and all the non-CO_2 intermediates/products of the

321 oxidation (CH_3OOH, CH_3OH, HCHO, and CO) are orders of magnitude more reactive toward OH than is

322 CH_4 (Atkinson and Arey, 2003). This large difference in precursor and intermediate/product oxidation

323 timescales allows the oxidations of intermediates/products (including CO, whose reaction rate constant

324 with OH is $\sim 2 \times 10^{-13}$ cm^3 $molecule^{-1}$ s^{-1}; Burkholder et al., 2015) to establish a steady state, whereby the

325 OHR of the intermediates/products is proportional to the concentration/OHR of CH_4. After $OH_{exp} \sim 10^{13}$

326 molecules cm^{-3} s, CH_4 concentration decay, and consequently that of all intermediates/products,

327 become significant, giving the OHR_{VOC} peak around 1×10^{13} molecules cm^{-3} s.

328   We also performed a simulation under a typical OFR condition. The OHR_{VOC} peak also appears

329 around 1×10^{13} molecules cm^{-3} s in this case for the same reasons discussed above, but its height is

330 almost twice that of the ambient case (Fig. S3). The OHR of CO in both cases is similar, while that of

331 CH_3OH is higher in the ambient case but those of CH_3OOH and HCHO are significantly higher in the OFR

332 case. This is because the relative importance of the various reactions involved in CH_4 oxidation (Scheme

333 S2) depends on the conditions in each reactor.

334   In the OFR case, OH and HO_2 concentrations are ~ 4 and ~ 3 orders of magnitude higher than

335 typical ambient values, respectively (Peng et al., 2015). The reactions of two intermediates, CH_3OOH

336 and HCHO, with OH and the reaction of the only major RO_2 involved, CH_3OO, with HO_2 are much faster

337 than their photolysis or the self-reaction of CH_3OO (Scheme S2). Neglecting organic photolysis and

338 CH_3OO self-reaction (and thus CH_3OH as a product of the latter), the mechanism of CH_4 oxidation can

339 be simplified to an OH-driven chain ($CH_4 \rightarrow CH_3OOH \rightarrow HCHO \rightarrow CO \rightarrow CO_2$) with a fast steady-state

340 branch on CH_3OOH ($CH_3OOH \leftrightarrow CH_3OO$). For a simple chain, as we show in Appendix A, the OHR of

341 precursor and that of each intermediate are equal. At the OHR_{VOC} peak, the OHR of HCHO and CO are

342 very close to that of CH_4, while that of CH_3OOH is larger, because the branch reaction $CH_3OOH + OH \rightarrow$

343 $CH_3OO + H_2O$ also contributes to OHR, but does not affect the chain (and hence the OHR of the

344 downstream species). With such an idealized chain mechanism, the OHR_{VOC} peak height equals the

345 precursor OHR multiplied by the number of steps needed to produce CO_2.

346   In contrast, the OHR_{VOC} peak height (and its composition) in the ambient case cannot be

9

347 explained by the simple chain. Both HCHO photolysis and CH_3OO self-reaction play a major role in the

348 oxidation in this case, and are significantly faster than the reactions in the simple chain (HCHO + OH

349 and $CH_3OO + HO_2$). In terms of the relationship of these two reactions with the chain, HCHO photolysis

350 bypasses HCHO + OH in converting HCHO to CO, while CH_3OO self-reaction bypasses CH_3OOH, in effect

351 short-circuiting the involvement of OH in the oxidation and hence lowering OHR_{VOC} (Appendix A). Since

352 the only reaction of CO is CO + OH, its OHR at the OHR_{VOC} peak is essentially unaltered.

353 **3.2   Decane**

354 **3.2.1   Ambient and OFR cases**

355 The evolution of OHR_{VOC} during the oxidation of another alkane, decane, under ambient and OFR

356 conditions exhibit a smaller difference and smaller peak enhancements than those in the methane

357 cases (Fig. 1), although the chain lengths of the decane oxidation to CO_2 should be much longer than

358 that of methane. The ambient cases with constant and diurnal solar radiation have almost the same

359 OHR_{VOC} evolution as a function of OH_{exp} (Figs. 1 and 2). ~~Contrary to the methane cases, OHR_{VOC} in all~~

360 ~~five decane simulations for OFR conditions is lower than that for ambient conditions.~~

361 These differences from the methane cases arise because a key assumption of the simple reaction

362 chain model, i.e., slow precursor decay allowing intermediates/products to build up and reach a steady

363 state, no longer holds in decane oxidation. <u>The main first-generation products, i.e., secondary decyl</u>

364 <u>hydroperoxides, react with OH only less-than-3-times more rapidly (in terms of the rate constant of the</u>

365 <u>whole molecule) than does decane, as the significant activation effect of the –OOH group only applies</u>

366 <u>to the α-H, and all other H atoms in this long chain alkyl, though less reactive, can be abstracted by OH</u>

367 <u>(Kwok and Atkinson, 1995; Aumont et al., 2005).</u>~~The main first-generation products, i.e., secondary~~

368 ~~decyl hydroperoxides, react with OH only < x3 more rapidly than does decane, as the significant~~

369 ~~activation effect of the –OOH group only applies to the α-H, and all other H atoms in this long chain~~

370 ~~alkyl can, though less reactive, be abstracted by OH (Kwok and Atkinson, 1995; Aumont et al., 2005).~~

371 When decyl hydroperoxides are present in significant amounts (OH_{exp} ~ $5x10^{10}$ molecules cm^{-3} s),

372 decane loss is also significant (Fig. 3). Also, oxidation of monohydroperoxides to ketones, their most

373 likely fate (due to the activated α-H), lowers OHR_{VOC}, as the oxidation removes the most activated H

374 (Kwok and Atkinson, 1995). The multifunctional products of further oxidation in the mid OH_{exp} range

375 (before ~$2x10^{11}$ molecules cm^{-3} s), mainly have -OOH and -CO- (Fig. 4), which do not further increase

376 OHR substantially with respect to monohydroperoxides, for similar reasons as the comparison of

377 monohydroperoxides with decane. After the OHR_{VOC} peak, the precursor is largely consumed and -

378 CH(OOH)- groups become increasingly oxidized to -CO- in both monohydroperoxides and

379 multifunctional hydroperoxides (Figs. 3 and 4), which rapidly decreases OHR_{VOC}. Since the decane

380 oxidation chain does not reach a steady state, it results in only limited OHR_{VOC} enhancement at peak.

381 ~~The differences between the ambient and OFR cases for decane oxidation are for different~~

382 ~~reasons than in the case of CH_4.~~ In the absence of steady state for the nodes (stable species) in the

383 decane oxidation chains (nodes far downstream insufficiently populated), organic photolysis and RO_2

384 self- and cross-reactions only help move OHR contributors to downstream nodes, but do not

385   significantly change their total concentrations. This is shown by the relatively small differences in the
386   composition of stable OHR contributors between the ambient and OFR cases (Fig. 3). The remarkable
387   difference between these cases is the contribution of RO_2 to OHR, which is as high as ~3 s^{-1} in the OFR
388   case shown in Fig. 3, while estimated to be only up to ~0.1 s^{-1} in the ambient case, given the RO_2
389   concentration in the simulation.

390   It is known that RO_2 + OH can be a significant RO_2 loss pathway in OFR, especially when OH and
391   HO_2 production is relatively strong (higher relative humidity (RH) and UV). We have previously advised
392   to avoid such conditions in low-NO chemistry based on simplified modeling, because of its high-NO-like
393   organic product (Peng et al., 2019). Here our chemically explicit modeling results show that the
394   limitation for OFR chemistry caused by RO_2 + OH may not be as serious as suggested by Peng et al.
395   (2019), at least in terms of OHR_{VOC} and, to some extent, of organic composition (Fig. 3). The condition
396   of the OFR case shown in Fig. 3 (30% RH, medium UV, and 10 s^{-1} initial OHR) is a compromise between
397   the goals of reaching an equivalent photochemical age of ~10 d, avoiding significant non-tropospheric
398   organic photolysis, and keeping a more atmospherically relevant RO_2 chemistry (Peng et al., 2016; Peng
399   et al., 2019; Peng and Jimenez, 2020). In this case, the fractional contribution of RO_2 + OH to RO_2 fate
400   is still sizable (>30%). However, the evolution of the composition of monofunctional species in this OFR
401   case before the OHR_{VOC} peak equivalent age is similar to that in the ambient case (Fig. 3), as
402   hydroperoxide production through RO_2 + HO_2 is still the main loss pathway of the first-generation RO_2
403   and RO produced from RO_2 + OH can also form ketones, i.e., the main second-generation products. The
404   other main fate of RO, i.e., isomerization, leads to slightly faster production of multifunctional species,
405   since the product of the recombination of the immediate product of this isomerization, i.e., an alkyl
406   radical, with O_2 is already a bifunctional RO_2. This isomerization also creates a hydroxyl group on the C
407   backbone, resulting in a relatively high share of hydroxyl in the functional groups of the multifunctional
408   species (Fig. 4).

409   Before the OHR_{VOC} peak, as OH_{exp} increases, carbonyls accumulate. They are prone to Norrish-
410   type photochemistry (Turro et al., 2009) which plays a major role in the OHR evolution after the OHR_{VOC}
411   peak in the ambient cases by breaking C10 species into smaller molecules (Fig. 3). Alkenes, which can
412   only be produced via Norrish Type II reaction in this case (Turro et al., 2009), are non-negligible OHR
413   contributors around 3×10^{11} molecules cm^{-3} s. A set of oxygenated C1 and C2 species are also largely
414   produced through organic photolysis followed by reactions with (O_2 and) HO_2. Organic photolysis, along
415   with OH reaction pathways, can also produce RO_2. Self- and cross-reactions of acylperoxy radicals,
416   which are formed in significant amounts in this OH_{exp} range, can rapidly generate alkoxy radicals
417   (Orlando and Tyndall, 2012), which may decompose subsequently (Ziemann and Atkinson, 2012). At
418   ~1×10^{12} molecules cm^{-3} s, the small species produced account for about half of OHR_{VOC} in the ambient
419   cases (Fig. 3). In the OFR cases, organic photolysis is usually much weaker than in the atmosphere (Peng
420   et al., 2016; Peng and Jimenez, 2020), as the negligible OHR of alkenes in the OFR case in Fig. 3 also
421   indicates. However, fragmentation of multifunctional species does not appear to be significantly
422   weaker in the OFR case than in the ambient case shown in Fig. 3. This is largely due to fast RO_2 + OH.

423 The reactions of acylperoxys with OH lead to direct fragmentation (Orlando and Tyndall, 2012). Highly

424 functionalized RO can also form from the reactions of multifunctional RO_2 with OH, and then often

425 rapidly decompose. RO_2 + OH also results in a major difference of the OFR case from the ambient case

426 at high equivalent ages (Fig. 3), i.e., lower (higher) OHR contribution from CH_3OOH (HCHO) in OFR than

427 in the atmosphere. Most CH_3OO reacts with OH to produce CH_3O then HCHO in the OFR case, leaving a

428 minor fraction of CH_3OO reacting with HO_2 to form CH_3OOH.

3.2.2 Chamber cases

430 ~~Two types of chamber simulations, with and without wall partitioning, are considered in this~~

431 ~~study. The latter have almost the same results as the ambient cases in terms of the evolution of OHR_{VOC}~~

432 ~~and its composition as a function of OH_{exp} (Fig. 1). Despite different spectra, sunlight and chamber lights~~

433 ~~cover the same wavelength range and usually generate oxidizing agent radicals (e.g., OH and HO_2) in~~

434 ~~similar amounts. Therefore, all key parameters are very similar between the ambient case with constant~~

435 ~~solar radiation and the chamber case (with 10 s^{-1} initial OHR) and without gas-wall partitioning.~~ Three

436 types of chamber simulations, without gas-particle-wall partitioning, with gas-particle partitioning only

437 (no wall), and with gas-particle-wall partitioning, are considered in this study. The first type has almost

438 the same results as the ambient cases in terms of the evolution of OHRVOC and its composition as a

439 function of OH_{exp} (Fig. 1). Despite different spectra, sunlight and chamber lights cover the same

440 wavelength range and usually generate oxidizing agent radicals (e.g., OH and HO_2) in similar amounts.

441 Therefore, all key parameters are very similar between the ambient case with constant solar radiation

442 and the chamber case (with 10 s^{-1} initial OHR) and without gas-particle-wall partitioning. This explains

443 the high similarities between the results of the ambient cases and the chamber cases without wall

444 partitioning. Unfortunately, the lack of wall partitioning is not realistic for current chambers.

445 The chamber cases with gas-particle-wall partitioning at lower initial OHR, which are realistic,

446 show very large deviations from the ambient cases that cannot be explained by gas-particle partitioning

447 only (Figs. 1, 3 and S4). These deviations are mostly due to wall partitioning of OVOCs around the OH_{exp}

448 of the OHR peak and at lower OH_{exp}. In this OH_{exp} range, the wall removes about half of the OHR of

449 decane oxidation intermediates/products (Figs. 1 and 2) and hence also almost removes the OHRVOC

450 peak in the relevant chamber cases (Fig. 1). In detail, some decyl hydroperoxides partition to the wall

451 in the chamber case shown in Fig. 3, as decyl is a relatively large alkyl and leads to hydroperoxides of

452 sufficiently low volatility to promote wall partitioning. The C10 ketones, usually of higher volatility than

453 the corresponding hydroperoxides, do not show significant wall partitioning (Fig. 3), while about half of

454 the multifunctional C10 species, of even lower volatility than the corresponding hydroperoxides, are

455 partitioned to the wall.

456 At higher OH_{exp} (>2x10^{11} molecules cm^{-3} s), more multifunctional species stay in the gas phase

457 or partition to the particle phase (Figs. 3 and S4). Those in the gas phase are formed via C10

458 fragmentation and are thus of higher volatility (Fig. 3). Those partitioned to the particle phase instead

459 of the wall are due to a higher organic aerosol concentration resulting from accumulation during a long

460 oxidation. The substantial partitioning of multifunctional species to aerosol and the wall also slows

12

down their oxidative evolution in the gas phase relative to the ambient cases (Fig. 4). The degree of oxidation of products partitioned to the particle phase increases since low OH_{exp}. This is due to a volatility fractionation caused by the lower ability of the particle phase to absorb condensable organic gases than that of the wall phase at this OH_{exp}. At low organic aerosol loading, the relative potential of particle partitioning to wall partitioning for organic gases of higher functionalization is higher than for those of lower functionalization.

At higher initial OHR (100 s-1), and hence higher organic aerosol loading, condensable gases have a significantly higher tendency of partitioning to the particle phase. The reduction of OHR of the higher initial OHR chamber case with aerosol partitioning only (no wall partitioning) relative to the purely gas-phase case is comparable to the lower initial OHR case with gas-particle-wall partitioning at low OH_{exp} (before the OHR peak) (Fig. S4). At high OH_{exp}, this OHR reduction is even stronger than in the lower initial OHR case with gas-particle-wall partitioning, as partitioning of OVOCs to the particle phase dominates over that to the walls.

As OH_{exp} increases and large multifunctional species are formed in increasing amounts from oxidation, their substantial partitioning to aerosol and the wall decreases the OHR of decane oxidation intermediates/products by a factor up to 8 around 1x1012 molecules cm-3 s compared to the chamber cases without gas-particle-wall partitioning (Figs. 2 and S4). At higher OHexp (long oxidation times) gas-phase concentrations of partitioning species decline, allowing reverse partitioning back from the particle phase and the wall which then serves as a source rather than a sink. As a result, the ratio of the OHR of oxidation intermediates/products in the chamber case with gas-particle-wall partitioning to that without this partitioning decreases (Fig. 2). The chamber cases with gas-wall partitioning, which are realistic, show very large deviations from the ambient cases (Figs. 1 and 3). These deviations are remarkably larger than those of the OFR cases, and are obviously due to wall partitioning of OVOCs. The wall removes more than half of the OHR of decane oxidation intermediates/products (Figs. 1 and 2) and hence also removes the OHR_{VOC} peak in the relevant chamber cases (Fig. 1). In detail, about half of decyl hydroperoxides partition to the wall in the chamber case shown in Fig. 3, as decyl is a relatively large alkyl and leads to hydroperoxides of sufficiently low volatility to promote wall partitioning. The C10 ketones, usually of higher volatility than the corresponding hydroperoxides, do not show significant wall partitioning (Fig. 3), while the multifunctional C10 species, of even lower volatility than the corresponding hydroperoxides, are almost completely partitioned to the wall. The multifunctional species that survive the wall partitioning at high OH_{exp} (~1×10^{12} molecules cm^{-3} s) are formed via C10 fragmentation and are thus of higher volatility (Fig. 3). The heavy wall partitioning of multifunctional species also significantly slows down their oxidative evolution in both the wall phase and the gas phase relative to the ambient cases (Fig. 4).

As OH_{exp} increases and large multifunctional species are formed in increasing amounts from oxidation, their near-complete partitioning to the wall decreases the OHR of decane oxidation intermediates/products by a factor up to 8 around 1×10^{12} molecules cm^{-3} s compared to the chamber cases without gas-wall partitioning (Fig. 2). At higher OH_{exp} (long oxidation times) gas-phase

503 3.2.3 OH and HO_x recycling ratios

504 As discussed above, we also compute OH (β_1) and HO_x (β_2) recycling ratios in decane oxidation.

505 Note that these quantities also include OH and HO_2 generated as a result of organic photolysis. The

506 differences in these recycling ratios between the simulated cases are relatively small. β_1 is close to 0 at

507 $OH_{exp} < \sim 1 \times 10^{10}$ molecules cm^{-3} s (Fig. 1), as the initial reaction of decane with OH only produces an RO_2

508 and subsequently C10 hydroperoxides, and no HO_x. Then β_1 undergoes a fast increase between $\sim 1 \times 10^{10}$

509 and 1×10^{11} molecules cm^{-3} s (Fig. 1), as the further oxidation of C10 hydroperoxides to ketones fully

510 recycles OH (R_1-CH(OOH)-R_2 + OH → R_1-CO-R_2 + H_2O + OH) in the ambient and chamber cases.

511 Nevertheless, β_1 only increases up to ~ 0.4 at this stage in the ambient and chamber cases, as oxidation

512 of C10 hydroperoxides to dihydroperoxy species and precursor oxidation also account for a substantial

513 fraction of OH loss but do not recycle it. In the OFR cases, β_1 only increases up to ~ 0.2–0.3 at this stage,

514 since RO_2 + OH starts to be active but does not recycle OH. Then, β_1 roughly plateaus up to $\sim 1 \times 10^{12}$

515 molecules cm^{-3} s, as the overall effect of the decrease in hydroperoxy concentration, reducing OH

516 recycling, and the increase in the concentration of acylperoxy, enhancing OH recycling through its

517 reaction with HO_2 (Orlando and Tyndall, 2012), is relatively small. Finally, β_1 gradually decreases to 0

518 (Fig. 1), as all OVOCs degrade to highly oxidized C1 species, i.e., HCHO, HCOOH, CO, which only have

519 HO_2 recycling but no OH recycling, and the unreactive CO_2.

520 The HO_x recycling ratio (β_2) in decane oxidation is similar to β_1 before $\sim 1 \times 10^{11}$ molecules cm^{-3} s

521 for the ambient and chamber cases, as only OH (but not HO_2) is recycled at this stage. β_2 is a little higher

522 in the OFR cases than in the other cases at this stage because of the HO_2 recycling by RO_2 + OH.

523 However, at higher OH_{exp}, β_2 continues to increase with OH_{exp} to a final value of 1 (Fig. 1). This difference

524 between β_1 and β_2 is by definition due to HO_2 recycling. Its significance rises in parallel with that of

525 organic photolysis, which can often produce HCO radicals and acylperoxy radicals. The former

526 extremely rapidly undergoes HCO + O_2 → CO + HO_2; the latter can rapidly convert peroxy radicals to

527 alkoxy radicals (Orlando and Tyndall, 2012), which may then react with O_2 to generate HO_2 (Ziemann

528 and Atkinson, 2012). At very high OH_{exp} (10^{12} – 10^{13} molecules cm^{-3} s), reactive highly oxidized small

529 VOCs are the dominant OHR contributors and many of them recycle HO_2 during their oxidation by OH

530 (Fig. 3). Finally, once CO becomes the only remaining OHR contributor, β_2 is 1.

531 3.3 m-Xylene

532 Most features in m-xylene oxidation can be explained based on similar discussions as for decane

533 oxidation in Section 3.2. OHR_{VOC} also has a maximum during the oxidation (Figs. 1 and S4), as most of

534 the direct products of m-xylene oxidation by OH, i.e., the unsaturated carbonyl (MXYEPOXMUC in MCM

535 v 3.2 notation, see Scheme S1), the unsaturated endo-cyclic peroxide (MXYBPEROOH~~MXYBIPERO2~~),

536 and xylenols, are more reactive toward OH than m-xylene. The OHR of these initial products is enhanced

14

much more during the oxidation of m-xylene than of decane, owing to the creation of C=C bonds in many post-aromatic (ring-opening) products, hence the OHR_{VOC} peak enhancement in m-xylene oxidation is larger than in decane oxidation. Because the reaction rate constant of m-xylene with OH slightly exceeds that of decane, the OHR_{VOC} peak in m-xylene oxidation occurs at slightly lower OH_{exp} than in decane oxidation (Fig. 1). In the OFR case under the same condition as the decane case shown in Fig. 3, the evolution of OHR of the stable organic species is again similar to that in the ambient case. And OHR_{VOC} is higher in the OFR case again mainly due to OHR from RO_2 (Fig. 1 and S4). Several main first- and second-generation products are already highly functionalized through fast O_2 addition (Scheme S1) and they are also often unsaturated and prone to further functionalization. Therefore, the degree of functionalization in saturated aliphatic multifunctional species is much higher in m-xylene than in decane oxidation (Fig. 4). Also, as several aromatic-scheme-specific reaction types occur in the early stages of m-xylene oxidation, e.g., endo O_2 addition (creating -OO- etc.) and ring-opening (creating -CO-, -CHO etc.), multifunctional species functionality is more diverse than in decane oxidation (Fig. 4). Photolysis again plays a role in species fragmentation and the production of highly oxidized C1 and C2 species after the OHR_{VOC} peak (Fig. S4).

At low OH_{exp} and that of the OHRVOC peak, particle and wall partitioning also substantially reduces the OHRVOC in the relevant chamber cases of m-xylene oxidation while the OHRVOC reduction due to partitioning to the particle phase is smaller than that due to the wall (Figs. 1, 2, S4 and S5). The precursor (m-xylene) is a C8 species and even many first-generation products of its oxidation are highly oxygenated (Scheme S1) lower-volatility species. The relative reduction of OHR of the intermediates/products also increases with OH_{exp} before the OH_{exp} of the OHR peak, as volatile species are oxidized and become more prone to wall partitioning (Figs. 2 and S4). At higher OH_{exp}, more condensed organics are partitioned to the particle phase because of high organic aerosol concentration (Fig. S4) and the wall and aerosol again serve as OVOC source (Fig. 2). Wall partitioning also substantially reduces the OHR_{VOC} in the relevant chamber cases of m-xylene oxidation (Figs. 1, 2 and S4). The precursor (m-xylene) is a C8 species and even many first-generation products of its oxidation are highly oxygenated (Scheme S1) lower-volatility species. The relative reduction of OHR of the intermediates/products also increases with OH_{exp} up to ~1×10^{12} molecules cm^{-3} s, as volatile species are oxidized and become more prone to wall partitioning (Fig. 2). At higher OH_{exp}, the wall again serves as an OVOC source (Fig. 2).

The evolution of β_1 and β_2 in m-xylene oxidation is somewhat different than in decane oxidation (Fig. 1). In the ambient cases, they are non-negligible even at OH_{exp} as low as 1×10^9 molecules cm^{-3} s (~0.05 and ~0.45, respectively). OH is mainly recycled from one of endo-cyclic peroxide routes (m-xylene + OH + 2O_2 → MXYBIPERO2; MXYBIPERO2 + HO$_2$ → MXYBPEROOH + O_2; MXYBPEROOH + OH → MXYOBPEROH + H_2O + OH (Scheme S1)), which involve various functional groups and open the possibility of radical recycling. The third step of this route is very fast (with a rate constant on the order of 10^{-10} cm^3 molecule^{-1} s^{-1}). Once the second step takes place, the third step contributes to OH recycling. However, in the OFR cases with strong water vapor photolysis (not in the other OFR cases), the third

575 step does not play a significant role and β_1 is ~0 at very low OH_{exp} (Fig. 1) due to the relatively slow

576 second step ($RO_2 + HO_2$).~~However, in the OFR cases with strong water vapor photolysis (not in the other~~

577 ~~OFR cases) and the chamber cases with gas-wall partitioning, the third step does not play a significant~~

578 ~~role and β_1 is ~0 at very low OH_{exp} (Fig. 1).~~ In the former cases, this is due to the relatively slow second

579 step ($RO_2 + HO_2$), while in the latter cases, the highly oxygenated compounds partition to the wall even

580 more rapidly (in hundreds of s; Krechmer et al., 2016) than their reactions with HO_x. Strong HO_2

581 recycling occurs in all simulated cases from the beginning of the oxidation (Fig. 1), since two of the three

582 major channels of m-xylene + OH (i.e., those forming MXYEPOXMUC and xylenol, respectively) produce

583 HO_2 as well.

584 ~~As more multifunctional species are formed (particularly through ring-opening) near the OH_{exp}~~

585 ~~of the peak OHR_{VOC}, HO_x recycling is also active, with β_1 increasing and β_2 remaining high (Fig. 1). There~~

586 ~~are a few peaks in β_1 and β_2 for certain chamber cases. The peak in β_2 for the chamber case with high~~

587 ~~initial OHR (100 s^{-1}) and no walls results from RO_2 cross-reactions, many of which produce alkoxy~~

588 ~~radicals that subsequently yield carbonyls and HO_2 through reactions with O_2 (Orlando and Tyndall,~~

589 ~~2012). RO_2 cross-reactions are significant in that OH_{exp} range also because i) high precursor~~

590 ~~concentration translates into higher RO_2 concentration and ii) acylperoxy radicals, whose reactions with~~

591 ~~other RO_2 are fast (Orlando and Tyndall, 2012), are rapidly formed from the oxidation of -CHO groups~~

592 ~~in the ring-opening products (Scheme S1). The peaks in the chamber cases with wall partitioning are~~

593 ~~caused by a small number of species (in particular methylglyoxal) sufficiently volatile to stay in the gas~~

594 ~~phase and thus have disproportionate influence on β_1 and β_2. Methylglyoxal photolysis and the reaction~~

595 ~~of HO_2 with $CH_3COCO(OO)$, i.e., the acylperoxy formed through methylglyoxal + OH, are largely~~

596 ~~responsible for the HO_2 and OH recycling at the OH_{exp} of the peaks. At higher OH_{exp}, calculated β_1 and~~

597 ~~β_2 become less reliable, since remaining apparent OHR contributors may in fact be persistent artifacts~~

598 ~~of the incompleteness of the (hand-written) m-xylene oxidation mechanism which may substantially~~

599 ~~bias β_1 and β_2 when the concentrations of remaining OHR contributors should be generally low.~~

600 ~~Therefore, we do not try to interpret the features in β_1 and β_2 at high OH_{exp} for m-xylene oxidation.~~As

601 more multifunctional species are formed (particularly through ring-opening) near the OH_{exp} of the peak

602 OHR_{VOC}, HO_x recycling is also active, with β_1 increasing and β_2 remaining high (Fig. 1). There is a high

603 peak in β_2 for the chamber case with high initial OHR (100 s^{-1}) and no aerosol or wall partitioning. It

604 results from RO_2 cross-reactions, many of which produce alkoxy radicals that subsequently yield

605 carbonyls and HO_2 through reactions with O_2 (Orlando and Tyndall, 2012). RO_2 cross-reactions are

606 significant in that OH_{exp} range also because i) high precursor concentration translates into higher RO2

607 concentration and ii) acylperoxy radicals, whose reactions with other RO_2 are fast (Orlando and Tyndall,

608 2012), are rapidly formed from the oxidation of -CHO groups in the ring-opening products (Scheme S1).

609 The chamber case with high initial OHR and gas-particle-wall partitioning does not have such a high β_2

610 peak, because of fast partitioning of the oxidation products containing -CHO groups to the aerosol and

611 wall phases, which significantly reduces acylperoxy radical concentration around the OH_{exp} of the peak

612 OHRVOC. At higher OH_{exp}, calculated β_1 and β_2 become less reliable, since remaining apparent OHR

contributors may in fact be persistent artifacts of the incompleteness of the (hand-written) m-xylene oxidation mechanism which may substantially bias β_1 and β_2 when the concentrations of remaining OHR contributors should be generally low. Therefore, we do not try to interpret the features in β_1 and β_2 at high OH_{exp} for m-xylene oxidation.

3.4 Isoprene

The most salient difference of the OHR_{VOC} evolution in the photooxidation of isoprene from that of the other precursors in this study is the lack of OHR_{VOC} peak in the isoprene cases (Figs. 1 and S5). The decrease in OHR_{VOC} all along this photooxidation is expected since the reaction of isoprene with OH is very fast (at 1×10^{-10} cm^3 molecule^{-1} s^{-1}; Atkinson and Arey, 2003) and all intermediates/products of this photooxidation react with OH more slowly than isoprene. The OHR_{VOC} of the intermediates/products peaks slightly after an OH_{exp} of 1×10^{10} molecules cm^{-3} s (Fig. 1). At this OH_{exp}, the main type of the first-generation products, oxygenated unsaturated species (e.g., isoprene-derived unsaturated hydroxyl hydroperoxides (ISOPOOH)), are largely produced from isoprene + OH and their loss rates (with rate constant with OH slightly lower than that of isoprene) reach the maxima (Fig. S5). Further oxidation leads to the loss of all C=C bonds in the isoprene C backbone and thus a substantial drop of the OHR of the molecule.

Before $OH_{exp} \sim 5 \times 10^{10}$ molecules cm^{-3} s in isoprene photooxidation, the main deviations from the ambient cases shown by the chamber cases with wall partitioning are again caused by wall partitioning of multifunctional species, but their relative magnitudes are different than in the photooxidations of decane and m-xylene, with the impacts of wall partitioning being smaller (Fig. S5). Oxygenated species derived from isoprene, a C5 species, should be generally more volatile and less prone to wall partitioning than those derived from decane and m-xylene. On the other hand, isoprene reacts with OH much more rapidly than do decane or m-xylene, creating a larger deviation from the steady state for RO_2 directly derived from isoprene and a more remarkable decrease in the OHR of the first-generation products (Fig. S5). In the OFR case shown in Fig. S5, RO_2 contributes negligibly to OHR_{VOC}, since many first-generation isoprene-derived RO_2 have other very fast loss pathways and the very fast decay of isoprene cannot sustain RO_2 production at $OH_{exp} > \sim 1 \times 10^{10}$ molecules cm^{-3} s.

~~After $OH_{exp} \sim 5 \times 10^{10}$ molecules cm^{-3} s, the deviation caused by chamber wall partitioning becomes more significant as highly oxidized and lower-volatility multifunctional species (Fig. 4) are formed in significant amounts (Figs. 2 and S5).~~ After $OH_{exp} \sim 5 \times 10^{10}$ molecules cm-3 s, the deviation caused by chamber wall partitioning becomes more significant as highly oxidized and lower-volatility multifunctional species (Fig. 4) are formed in significant amounts (Figs. 2 and S6). However, aerosol partitioning does not become more significant as in the chamber cases of isoprene oxidation aerosol formation is always so small that partitioning to the particle phase never competes with that to the walls. At very high OH_{exp}, the wall again acts as a source of OVOCs in isoprene oxidation, as in those of the other precursors (Fig. 2). The deviations of OFR cases from the ambient cases are mainly caused by RO_2 + OH and lack of organic photolysis. These two effects lead to too much HCHO produced and inefficient production of other C1 and C2 species (Fig. S5).

651   To test whether one of the issues, i.e., lack of organic photolysis in OFR, can be mitigated by

652   adding tropospherically-relevant UV sources, we perform two additional simulations. Adding the

653   emissions corresponding to high Hg lamp setting with five times the UV of the CU Chamber (a rough

654   upper limit for experimental implementation) has negligible effect (Fig. S6). To reach a ratio between

655   tropospherically-relevant UV (UVA+UVB) intensity and OH concentration similar to that in the ambient

656   case with constant sunlight requires addition of a chamber light ~10000 times stronger than the CU

657   Chamber light. Such a strong UV source is obviously not realistic, and, while it does increase both early

658   organic photolysis and the relative contribution of C1 and C2 photoproducts to OHR_{VOC} around $2x10^{11}$

659   molecules cm^{-3} s (Fig. S6), it increases the deviation of this OFR case from the ambient cases at very

660   high OH_{exp}, where oxidation of C1 and C2 species to CO proceeds much more rapidly than in the

661   atmosphere.

662   Product functionality in isoprene oxidation is more diverse than in decane oxidation (Fig. 4). This

663   is due to both the propensity of the isoprene C=C bonds to addition of various groups, and the active

664   isomerization of isoprene oxidation intermediates (Wennberg et al., 2018). Notably, epoxy groups in

665   species such as isoprene-derived epoxydiol (IEPOX) account for a large fraction of saturated product

666   functionality (Fig. 4), particularly at OH_{exp} on the order of 10^{10} molecules cm^{-3} s. In the gas phase of the

667   chamber cases with wall partitioning, the overwhelming majority of saturated multifunctional organic

668   molecules are IEPOX up to $1x10^{11}$ molecules cm^{-3} s (Fig. 4), as more highly-oxidized species mostly

669   partition to the wall.

670   IEPOX formation from isoprene-derived hydroperoxide (ISOPOOH) oxidation by OH (ISOPOOH +

671   OH → IEPOX + OH) leads to the peak of OH recycling around $3x10^{10}$ molecules cm^{-3} s (Fig. 1). OH

672   recycling is active even at very low OH_{exp} ($1x10^9$ molecules cm^{-3} s) because a significant amount of

673   ISOPOOH forms early and can recycle OH through its oxidation, except in the OFR cases with strong

674   water vapor photolysis, where ISOPOOH cannot be efficiently formed from first-generation RO_2. HO_2

675   recycling is also active in the entire course of the photooxidation (Fig. 1), because of a number of

676   isomerization and photolysis pathways that form alkoxy radicals and highly oxidized C1 species such as

677   HCOOH, HCHO, and CO at very high OH_{exp} (Fig. S5).

678   **3.5   Trends in OHR per C atom**

679   To explore some general trends of OHR evolution in VOC photooxidation, simulations are

680   performed for the ambient cases with constant UV for two additional alkanes between methane and

681   decane, i.e., butane and heptane. The results of these simulations are compared to the existing

682   analogous cases in Fig. 5. For all cases, the OHR_{VOC} peak height decreases and the OH_{exp} of the OHR_{VOC}

683   peak shifts towards lower OH_{exp}, as the C number of the precursor alkane increases. This can be

684   explained by the fact that the OH rate constants of these alkanes increase with C number, and suggests

685   a possible general trend between OHR peak location and C number.

686   To explore these trends further, we calculate the OHR per unit starting concentration of C atom

687   (in the precursor) in all ambient cases with constant UV in this study (Fig. 5b). In this study, CO_2 is not

688   included initially but produced during the oxidation. Therefore, C atoms in the produced CO_2 are taken

689 into account in the calculation of OHR per C atom. For real atmospheric cases, initial CO_2 is present but

690 should not be considered in this calculation. Note that OHR per C atom has a unit of cm^3 $atom^{-1}$ s^{-1} and

691 represents the average contribution to the rate constant with OH of all considered C atoms. Despite

692 large differences among the reactivities of these precursors, the OHR per C atom in the simulations of

693 all precursors but methane converges near an OH_{exp} of $3x10^{11}$ molecules cm^{-3} s, and then follows a very

694 similar downward trend (Fig. 5b). This OH_{exp} value is roughly where saturated multifunctional species

695 have their maximal relative contribution to the OHR_{VOC} (Figs. 3 and S5). Even in the ambient cases of m-

696 xylene oxidation, saturated multifunctional species also account for about half of OHR_{VOC} when the

697 contribution of aromatics, some of which may artificially persist due to mechanism incompleteness, is

698 excluded (Fig. S4). Also, at OH_{exp} > ~$3x10^{11}$ molecules cm^{-3} s, a C atom in saturated multifunctional

699 species on average has at least 0.3 functional groups in the ambient cases (Fig. 4), and the functional

700 group composition is relatively diverse at this OH_{exp}. Therefore, the convergence value of OHR per C

701 atom of ~$2x10^{-12}$ cm^3 $atom^{-1}$ s^{-1} at ~$3x10^{11}$ molecules cm^{-3} s can be largely regarded as a relatively

702 invariant average of those of secondary H and α-H of various O-containing functional groups. Note that

703 this average is for low-NO conditions and can be lower at high NO due to deactivating effects of N-

704 containing groups formed during oxidation (Isaacman-VanWertz and Aumont, 2021).

705   Before the convergence, isoprene has the highest OHR per C atom (on the order of 10^{-11} cm^3

706 $atom^{-1}$ s^{-1}) among the precursors and intermediates/products (Fig. 5b), because of its conjugated C=C

707 bonds. The OHR per C atom of its first-generation oxidation products is slightly lower and close to that

708 of the oxidation intermediates/products of m-xylene, as the main contributors in both cases are

709 oxygenated monoalkenes. The average OHR per C atom of the studied alkanes increases with C number

710 (Fig. 5b), with the upper limit around $1x10^{-12}$ cm^3 $atom^{-1}$ s^{-1} consistent with Kwok and Atkinson (1995),

711 since the less-reactive -CH_3 groups (with OHR per C atom of ~$1x10^{-13}$ cm^3 $atom^{-1}$ s^{-1}) contribute

712 proportionally less to molecular OHR as C number increases. Conversely, the early-stage products of

713 alkane oxidation (mainly alkyl monohydroperoxides) show higher average OHR per C atom for shorter

714 molecules (Fig. 5b), owing to the activating (increasing OHR) contribution of the -OOH group.

715   Following the convergence of OHR per C atom, this quantity in all non-methane ambient cases

716 in this study sees a similar decay (Fig. 5b). This coincides with multifunctional species broken into small

717 highly oxidized C1 and C2 compounds. Although among them there are species with OHR per C atom >

718 $5x10^{-12}$ cm^3 $atom^{-1}$ s^{-1} (e.g., CH_3OOH, CH_3CHO, and HCHO), the average OHR per C atom of these C1 and

719 C2 species are mainly governed by those reacting more slowly (e.g., HCOOH and particularly CO) and

720 hence reaching higher concentrations amid the fast decay of multifunctional species. The similar fast

721 drop of OHR per C atom after OH_{exp}~$1x10^{12}$ molecules cm^{-3} s for various precursors implies a transition

722 from OHR from saturated multifunctional molecules to OHR from CO before the final oxidation to CO_2

723 (which has zero OHR).

724 **3.6   Total OH consumption for each precursor**

725   Integrating OHR per C atom over OH_{exp} allows us to assess the average number of OH molecules

726 consumed by each C atom during the entire course of oxidation. This quantity can also be apportioned

727   to the contributions of different OH reactants (Fig. 6). Due to incomplete oxidation of several species,

728   especially CO, the value of this quantity for an oxidation with all C atoms ending up with CO_2 should be

729   higher than those at simulation end (OH_{exp}~4×10^{12} molecules cm^{-3} s). We correct this in Fig. 6 by

730   including additional contribution of CO to make its total contribution 1, since CO, the typical

731   penultimate product, consumes one OH molecule in its final oxidation, but is still present in significant

732   quantities at the end of our simulations. Thus, each C atom reacts with OH ~3 times in the course of the

733   oxidation of isoprene and decane to CO_2 (Fig. 6). A simplistic and chemically intuitive explanation for

734   this number is that the average oxidation state ($\overline{OS_C}$) of both isoprene and decane C atoms is ~-2, and

735   needs to increase to the value of +4 in CO_2 at the end of the oxidation. A C1 unit reacting once with OH

736   likely increases its $\overline{OS_C}$ by ~2. This increase is usually realized by an abstraction of H atom by OH or an

737   addition of OH ($\overline{OS_C}$+ 1), followed by an abstraction of H atom by O_2 or an addition of O_2 ($\overline{OS_C}$+ 1). Note

738   that ~3 OH consumed per C atom oxidized to CO_2 is likely an upper limit, since the mechanisms in this

739   study do not include RO_2 autoxidation (Crounse et al., 2013; Ehn et al., 2014), which reduces the

740   number of OH needed for complete VOC oxidation. Also, in a real low-NO environment, NO is still

741   present in low concentrations and converts RO_2 to RO. RO may undergo H abstraction through

742   isomerization or reaction with O_2, which also lowers the number of OH needed, although the effect is

743   usually small.

744   ~~The surprisingly large contribution of hydroperoxy xylenol ($C_8H_{10}O_3$) to OH consumed per C atom~~

745   ~~in m-xylene oxidation (Fig. 6) is an artifact of mechanism incompleteness. This species may undergo an~~

746   ~~abstraction of the H atom in its -OOH group by OH. The resulting RO_2 may be converted back to it~~

747   ~~through a reaction with HO_2. The lack of efficient exit channels from this interconversion artificially~~

748   ~~sustains it for an extended period, leading to inflated OH consumption.~~The number of OH consumed

749   per C atom in m-xylene oxidation is slightly lower than 3 (Fig. 6) because of the multiple addition of O_2

750   following a single OH addition in the initiation reaction, i.e., m-xylene + OH.

751 **4   Summary and conclusions**

752   Using the fully explicit GECKO-A model, we simulated OHR evolution in the photooxidation of

753   several types of VOCs (i.e., alkane, alkene, and aromatic) without NO until very high equivalent

754   photochemical ages (>10 d) under a variety of conditions (in the atmosphere, chamber, and OFR). We

755   analyzed the simulations in detail and found a number of common features as well as some differences

756   resulting from certain precursors. These features are summarized below:

757   -   All simulated non-methane cases very roughly follow this general oxidation chain pattern: precursor

758   → first-generation products → (second-generation products →) multifunctional species → highly

759   oxidized C1 and C2 species → CO (or HCOOH) → CO_2. These species are generally not at steady

760   state and gain significance/predominance one after another in the entire course of oxidation.

761   Simulation results suggest that fragmentation products are not formed in significant amounts until

762   the late stage of the oxidation, which would be a key difference from studies of OHR evolution in

763   high-NO VOC oxidation (Nakashima et al., 2012; Sato et al., 2017).

764   -   In methane oxidation, the intermediates do not gain dominance in sequence. Instead, they

765 simultaneously increase as the oxidation proceeds, then simultaneously decrease when the

766 methane decay becomes significant. The OHR evolution in methane oxidation is close to the

767 idealized steady-state chain model, as the reaction of methane with OH is orders of magnitude

768 slower than those of its oxidation intermediates, which allows the intermediates to reach their

769 steady state.

770 The following discussion refers to the non-methane cases.

771 - Where different types of species dominate OHR_{VOC} in sequence, OHR_{VOC} increases after the current

772 dominant type converts to one with a higher average OHR per C atom, and vice versa.

773 Photooxidations of alkanes and aromatics follow the increasing trend from precursor to saturated

774 multifunctional species (via alkyl monohydroperoxides) and from precursor to unsaturated

775 oxygenated species, respectively. The increase in aromatic oxidation is likely to be more significant,

776 since unsaturated oxygenated species are more reactive than saturated multifunctional species.

777 The conversions from multifunctional species to CO_2 lead to a decay of OHR_{VOC} in both alkane and

778 aromatic photooxidations. OHR_{VOC} in alkene photooxidation is likely to always drop rapidly during

779 C=C bond oxidation and more slowly afterwards.

780 - A relatively weak enhancement of OHR per C atom of a C atom with -OOH substitution can explain

781 the large range spanned by the precursors and their intermediates/products in this study at low

782 OH_{exp}. ~~C atoms in >C=C<, -CH$_2$-, and -CH$_3$ have OHR per C atom on the order of 10^{-11}, 10^{-12}, and 10^{-}~~

783 ~~^{13} cm^3 atom^{-1} s^{-1}, respectively. Together with these values, a relatively weak enhancement of OHR~~

784 ~~per C atom of a C atom with -OOH substitution can explain the large range spanned by the~~

785 ~~precursors and their intermediates/products in this study at low OH_{exp}.~~ Around an OH_{exp} of 3×10^{11}

786 molecules cm^{-3} s, precursors are largely converted to saturated multifunctional species (e.g., by

787 addition to C=C bonds in unsaturated precursors and abstraction of H atoms in saturated

788 precursors), and the reactive mixtures of those precursors thus have similar OHR per C atom. They

789 then all follow the course: multifunctional species → highly oxidized C1 and C2 species → CO (or

790 HCOOH) → CO_2 and show similar decays of OHR per C atom.

791 - In decane and isoprene oxidation, our simulations show that each C atom consumes at most ~3 OH

792 molecules in the course of its oxidation to CO_2. This can be simplistically explained as 3 occurrences

793 of oxidation by OH that increase, by 2 each time, the $\overline{OS_C}$ of decane and isoprene (~-2) to that of

794 CO_2 (+4). The total number of OH consumed by each C atom is likely to be lower when RO_2

795 autoxidation can be included in the mechanism generation.

796 In general, the OHR evolution differences resulting from different precursors are larger than those due

797 to different conditions. The difference in OHR_{VOC} between the ambient cases with constant and

798 diurnal sunlight is small. Nevertheless, physical conditions may still lead to significant differences,

799 which are summarized below:

800 - In current chambers, gas-wall partitioning can be a prominent issue that causes substantial wall

801 partitioning of certain OVOCs of lower volatility, depending on the chemical system under study.

802 The clearest example in this study is the substantial wall losses of C10 multifunctional species from

803   the gas phase in decane oxidation, and hence the remarkably lowered OHRVOC peak height in the

804   chamber simulation. ~~In chambers, gas-wall partitioning can be a prominent issue that causes~~

805   ~~substantial wall partitioning of certain OVOCs of lower volatility. The clearest example in this study~~

806   ~~is the near-complete removal of C10 multifunctional species from the gas phase in decane~~

807   ~~oxidation, and hence the disappearance of the OHR$_{VOC}$ peak.~~ The wall also preferentially absorbs

808   more oxidized (and thus lower-volatility) species, which alters the functional composition of gas-

809   phase multifunctional species. The wall can even serve as a source of multifunctional species at very

810   high OH$_{exp}$, when the gas-phase concentrations of those species are very low. The magnitude of the

811   effects of wall partitioning also depends on the size of the precursor, with the oxidation of larger

812   precursors in chambers suffering larger impacts of wall partitioning.

813   -   The strong wall losses have important implications, as they can change our modeling results

814   substantially. Systematic OVOC gas-particle-wall partitioning corrections must be made for low-NO

815   oxidation chamber experiments that study OHR$_{VOC}$. In case of large precursors, highly chemically

816   explicit modeling will likely be necessary to infer the OHR of multifunctional species, which may

817   account for a large fraction of missing reactivity but suffer substantial wall losses. Although the few

818   existing chamber studies on OHR$_{VOC}$ evolution were all under high-NO conditions, which may result

819   in more fragmentation and higher-volatility products, the magnitude of wall partitioning of large

820   multifunctional species in this study is so substantial that we believe this effect would also be

821   important at high NO. Schwantes et al. (2017) considered wall partitioning in their modeling of o-

822   cresol oxidation based on MCM v3.3.1 but still could not achieve good agreement with the

823   measurements for a number of products. Considering this, one should not assume that it is

824   appropriate to neglect gas-particle-wall partitioning in high-NO chamber experiments, just based

825   on agreement between the high-NO chamber experiments and modeling with MCM-based

826   schemes and without gas-particle-wall partitioning corrections. Even for OHR studies with less

827   surface loss issues, e.g., ambient studies, a combination of gas-phase-only OHR measurement and

828   modeling may still not be adequate as reduction of OHR due to OVOC condensation on aerosols can

829   also be significant in some situations (Fig. S4). Therefore, condensed phases (particle and wall) need

830   to be included in future OHR studies to better assess the deviation of the actual OHR from a purely

831   gas-phase picture.~~Systematic OVOC wall partitioning corrections must be made for low-NO~~

832   ~~oxidation chamber experiments that study OHR$_{VOC}$. In case of large precursors, highly chemically~~

833   ~~explicit modeling will likely be necessary to infer the OHR of multifunctional species, which may~~

834   ~~account for a large fraction of missing reactivity but suffer near-complete wall losses. Although the~~

835   ~~few existing chamber studies on OHR$_{VOC}$ evolution were all under high-NO conditions, which may~~

836   ~~result in more fragmentation and higher-volatility products, the magnitude of wall partitioning of~~

837   ~~large multifunctional species in this study is so substantial that we believe this magnitude would~~

838   ~~also be important at high NO. Schwantes et al. (2017) considered wall partitioning in their modeling~~

839   ~~of o-cresol oxidation based on MCM v3.3.1 but still could not achieve good agreement with the~~

840   ~~measurements for a number of products. Considering this, one should not assume that it is~~

- OFR has two issues under certain conditions that can cause deviations from the ambient cases in terms of OHR_{VOC}. Strong RO_2 + OH may significantly contribute to OHR_{VOC}. Interestingly, this type of reaction does not seem to be able to substantially alter the composition of OHR_{VOC}. before the OHR_{VOC} peak. Besides, the conditions resulting in strong water vapor photolysis have already been identified as those leading to atmospherically irrelevant RO_2 chemistry in low-NO OFR in previous studies (Peng et al., 2019; Peng and Jimenez, 2020). As long as OFR users follow the guidelines for experimental planning provided in those studies (and use a much lower UV lamp setting), strong RO_2 + OH can be avoided, as shown in Fig. 1.

- The other main issue of OFR is lack of efficient organic photolysis, particularly at high OH_{exp}, when multifunctional species break into highly oxidized C1 and C2 compounds. This problem has been highlighted in previous studies (Peng et al., 2016; Peng and Jimenez, 2020) and been shown again in the present work to be extremely difficult to avoid if a high OH_{exp} is desired. However, the conversion of multifunctional species into highly oxidized C1 and C2 species may not be much slower in OFR than in the atmosphere, since RO_2 + OH, leading to RO formation and subsequently its decomposition, may also play a major role in this conversion. This also results in significantly higher (lower) production of HCHO (CH_3OOH) in OFR than in the atmosphere at high equivalent ages.

With all the key findings in this study presented above, we believe that we have, to some extent, addressed the issues of "missing reactivity", of model limitations, and of OHR in remote areas for OHR studies raised by Williams and Brune (2015). With the fully explicit GECKO-A model, we speciated the likely source of the "missing reactivity", i.e., multifunctional OVOCs. A contrast between the technical issues in some isoprene and m-xylene simulations and the high consistency in the other cases highlights the importance of the completeness of the mechanism (even beyond the MCM level) in OHR-related modeling studies. Substantial wall partitioning of OVOCs in some chamber experiments highlights the importance of better constraining "gas-to-surface deposition terms''. More studies, both modeling (with highly chemically explicit mechanisms) and experimental (particularly low-NO), are needed to achieve better model-experiment closure. Finally, this study may have opened up the possibility of parameterizing the OHR evolution in (at least low-NO) VOC photooxidation as a function of OH_{exp} only with the often-available knowledge on the first- and second-generation products and the relevant SARs such as Kwok and Atkinson (1995), as the OHR evolution beyond multifunctional species has been shown to be similar for most VOC oxidations. This parametrization may be utilized in regional and global models to better constrain OHR at high equivalent photochemical ages, e.g., in remote regions.

888

Appendix A: The effect on OH reactivity of non-OH reactions in an OH-driven reaction chain

890 1) Consider the following reaction chain, where OH is the only oxidant:

891 $A_1 + OH \rightarrow A_2$, k_1

892 $A_2 + OH \rightarrow A_3$, k_2

893 $A_3 + OH \rightarrow A_4$, k_3

894 …(etc.)

895 At steady state, $k_1[A_1][OH] = k_2[A_2][OH] = k_3[A_3][OH] =…= C$ (C is a constant).

896 Then OHR due to individual species, OHR_i, is equal to $C/[OH]$ and is identical for all species.

897 2) Consider a parallel conversion of A_1 to A_2 by a means other than reaction with OH:

898 $A_1 + OH \rightarrow A_2$, k_1

899 $A_1 + B \rightarrow A_2$, k_1', $B \neq OH$
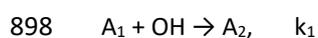
900 At steady state, $k_1[A_1][OH] + k_1'[A_1][B] = C$.

901 Therefore, $OHR_{A1} = k_1[A_1] < C/[OH]$.

902 3) Now consider a reaction converting A_1 directly to A_3 occurring in parallel to reaction chain 1),

903 $A_1 + D \rightarrow A_3$, k_1'', $D \neq OH$

904 $A_1 + OH \rightarrow A_2$, k_1

905 $A_2 + OH \rightarrow A_3$, k_2
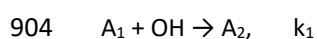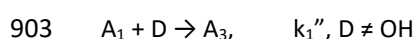
906 At steady state, $k_1''[A_1][D] + k_2[A_2][OH] = C$

907 And $OHR_{A1} < C/[OH]$, since $k_1[A_1][OH] = k_2[A_2][OH]$.

908

Code/Data availability

910 The chemical mechanisms generated and the outputs of the GECKO-A simulations in this study are
911 available upon request.
912

Author contribution

918

Conflicts of interest

There are no conflicts to declare.

Acknowledgements

928 **References**

929 Atkinson, R. and Arey, J.: Atmospheric Degradation of Volatile Organic Compounds, Chem. Rev.,
930 103(12), 4605–4638, doi:10.1021/cr0206420, 2003.

931 Aumont, B., Szopa, S. and Madronich, S.: Modelling the evolution of organic carbon during its gas-phase
932 tropospheric oxidation: development of an explicit model based on a self generating approach, Atmos.
933 Chem. Phys., 5(9), 2497–2517, doi:10.5194/acp-5-2497-2005, 2005.

934 Ausloos, P. J. and Lias, S. G.: Photochemistry in the Far Ultraviolet, Annu. Rev. Phys. Chem., 22(1), 85–
935 107, doi:10.1146/annurev.pc.22.100171.000505, 1971.

936 Bloss, C., Wagner, V., Jenkin, M. E., Volkamer, R., Bloss, W. J., Lee, J. D., Heard, D. E., Wirtz, K., Martin-
937 Reviejo, M., Rea, G., Wenger, J. C. and Pilling, M. J.: Development of a detailed chemical mechanism
938 (MCMv3.1) for the atmospheric oxidation of aromatic hydrocarbons, Atmos. Chem. Phys., 5(3), 641–
939 664, doi:10.5194/acp-5-641-2005, 2005.

940 Brune, W. H.: The Chamber Wall Index for Gas–Wall Interactions in Atmospheric Environmental
941 Enclosures, Environ. Sci. Technol., 53(7), 3645–3652, doi:10.1021/acs.est.8b06260, 2019.

942 Burkholder, J. B., Sander, S. P., Abbatt, J., Barker, J. R., Huie, R. E., Kolb, C. E., Kurylo, M. J., Orkin, V. L.,
943 Wilmouth, D. M. and Wine, P. H.: Chemical Kinetics and Photochemical Data for Use in Atmospheric
944 Studies: Evaluation Number 18, Pasadena, CA, USA. [online] Available from:
945 http://jpldataeval.jpl.nasa.gov/, 2015.

946 Camredon, M., Aumont, B., Lee-Taylor, J. and Madronich, S.: The SOA/VOC/NO$_x$ system: an explicit
947 model of secondary organic aerosol formation, Atmos. Chem. Phys., 7(21), 5599–5610,
948 doi:10.5194/acp-7-5599-2007, 2007.

949 Chameides, W., Lindsay, R., Richardson, J. and Kiang, C.: The role of biogenic hydrocarbons in urban
950 photochemical smog: Atlanta as a case study, Science (80-.)., 241(4872), 1473–1475,
951 doi:10.1126/science.3420404, 1988.

952 Crounse, J. D., Nielsen, L. B., Jørgensen, S., Kjaergaard, H. G. and Wennberg, P. O.: Autoxidation of
953 organic compounds in the atmosphere, J. Phys. Chem. Lett., 4, 3513–3520, doi:10.1021/jz4019207,
954 2013.

955 Ehn, M., Thornton, J. a, Kleist, E., Sipilä, M., Junninen, H., Pullinen, I., Springer, M., Rubach, F., Tillmann,
956 R., Lee, B., Lopez-Hilfiker, F., Andres, S., Acir, I.-H., Rissanen, M., Jokinen, T., Schobesberger, S.,
957 Kangasluoma, J., Kontkanen, J., Nieminen, T., Kurtén, T., Nielsen, L. B., Jørgensen, S., Kjaergaard, H. G.,
958 Canagaratna, M., Maso, M. D., Berndt, T., Petäjä, T., Wahner, A., Kerminen, V.-M., Kulmala, M.,
959 Worsnop, D. R., Wildt, J. and Mentel, T. F.: A large source of low-volatility secondary organic aerosol,
960 Nature, 506(7489), 476–479, doi:10.1038/nature13032, 2014.

961 Cohen, A. J., Brauer, M., Burnett, R., Anderson, H. R., Frostad, J., Estep, K., Balakrishnan, K., Brunekreef,
962 B., Dandona, L., Dandona, R., Feigin, V., Freedman, G., Hubbell, B., Jobling, A., Kan, H., Knibbs, L., Liu,
963 Y., Martin, R., Morawska, L., Pope, C. A., Shin, H., Straif, K., Shaddick, G., Thomas, M., van Dingenen, R.,
964 van Donkelaar, A., Vos, T., Murray, C. J. L. and Forouzanfar, M. H.: Estimates and 25-year trends of the
965 global burden of disease attributable to ambient air pollution: an analysis of data from the Global
966 Burden of Diseases Study 2015, Lancet, 389(10082), 1907–1918, doi:10.1016/S0140-6736(17)30505-6,
967 2017.

968 Fuchs, H., Hofzumahaus, A., Rohrer, F., Bohn, B., Brauers, T., Dorn, H. P., Haseler, R., Holland, F.,
969 Kaminski, M., Li, X., Lu, K., Nehr, S., Tillmann, R., Wegener, R., and Wahner, A.: Experimental evidence
970 for efficient hydroxyl radical regeneration in isoprene oxidation, Nature Geoscience, 6, 1023-1026,
971 doi:10.1038/Ngeo1964, 2013.

972 Fuchs, H., Novelli, A., Rolletter, M., Hofzumahaus, A., Pfannerstill, E. Y., Kessel, S., Edtbauer, A.,
973 Williams, J., Michoud, V., Dusanter, S., Locoge, N., Zannoni, N., Gros, V., Truong, F., Sarda-Esteve, R.,
974 Cryer, D. R., Brumby, C. A., Whalley, L. K., Stone, D., Seakins, P. W., Heard, D. E., Schoemaecker, C.,
975 Blocquet, M., Coudert, S., Batut, S., Fittschen, C., Thames, A. B., Brune, W. H., Ernest, C., Harder, H.,
976 Muller, J. B. A., Elste, T., Kubistin, D., Andres, S., Bohn, B., Hohaus, T., Holland, F., Li, X., Rohrer, F.,
977 Kiendler-Scharr, A., Tillmann, R., Wegener, R., Yu, Z., Zou, Q. and Wahner, A.: Comparison of OH
978 reactivity measurements in the atmospheric simulation chamber SAPHIR, Atmos. Meas. Tech., 10(10),

979   4023–4053, doi:10.5194/amt-10-4023-2017, 2017.

980   George, I. J. and Abbatt, J. P. D.: Heterogeneous oxidation of atmospheric aerosol particles by gas-phase
981   radicals., Nat. Chem., 2(9), 713–22, doi:10.1038/nchem.806, 2010.

982   Haagen-Smit, A. J.: Chemistry and Physiology of Los Angeles Smog, Ind. Eng. Chem., 44(6), 1342–1346,
983   doi:10.1021/ie50510a045, 1952.

984   Hallquist, M., Wenger, J. C., Baltensperger, U., Rudich, Y., Simpson, D., Claeys, M., Dommen, J.,
985   Donahue, N. M., George, C., Goldstein, A. H., Hamilton, J. F., Herrmann, H., Hoffmann, T., Iinuma, Y.,
986   Jang, M., Jenkin, M. E., Jimenez, J. L., Kiendler-Scharr, A., Maenhaut, W., McFiggans, G., Mentel, T. F.,
987   Monod, A., Prevot, A. S. H., Seinfeld, J. H., Surratt, J. D., Szmigielski, R. and Wildt, J.: The formation,
988   properties and impact of secondary organic aerosol: current and emerging issues, Atmos. Chem. Phys.,
989   9(14), 5155–5236, 2009.

990   Hodzic, A., Campuzano-Jost, P., Bian, H., Chin, M., Colarco, P. R., Day, D. A., Froyd, K. D., Heinold, B., Jo,
991   D. S., Katich, J. M., Kodros, J. K., Nault, B. A., Pierce, J. R., Ray, E., Schacht, J., Schill, G. P., Schroder, J. C.,
992   Schwarz, J. P., Sueper, D. T., Tegen, I., Tilmes, S., Tsigaridis, K., Yu, P. and Jimenez, J. L.: Characterization
993   of organic aerosol across the global remote troposphere: a comparison of ATom measurements and
994   global chemistry models, Atmos. Chem. Phys., 20(8), 4607–4635, doi:10.5194/acp-20-4607-2020, 2020.

995   Isaacman-VanWertz, G. and Aumont, B.: Impact of organic molecular structure on the estimation of
996   atmospherically relevant physicochemical parametersImpact of structure on the estimation of
997   atmospherically relevant physicochemical parameters, Atmos. Chem. Phys., 21(8), 6541-6563,
998   doi:10.5194/acp-21-6541-2021, 2021. Discuss., https://doi.org/10.5194/acp-2020-1038, in review,
999   2020.

1000   Jenkin, M. E., Saunders, S. M., Wagner, V. and Pilling, M. J.: Protocol for the development of the Master
1001   Chemical Mechanism, MCM v3 (Part B): tropospheric degradation of aromatic volatile organic
1002   compounds, Atmos. Chem. Phys., 3(1), 181–193, doi:10.5194/acp-3-181-2003, 2003.

1003   Jenkin, M. E., Young, J. C. and Rickard, A. R.: The MCM v3.3.1 degradation scheme for isoprene, Atmos.
1004   Chem. Phys., 15(20), 11433–11459, doi:10.5194/acp-15-11433-2015, 2015.

1005   Kang, E., Root, M. J., Toohey, D. W. and Brune, W. H.: Introducing the concept of Potential Aerosol Mass
1006   (PAM), Atmos. Chem. Phys., 7(22), 5727–5744, doi:10.5194/acp-7-5727-2007, 2007.

1007   Keller-Rudek, H., Moortgat, G. K., Sander, R. and Sörensen, R.: The MPI-Mainz UV/VIS Spectral Atlas of
1008   Gaseous Molecules of Atmospheric Interest, [online] Available from: www.uv-vis-spectral-atlas-
1009   mainz.org (Accessed 26 March 2019), 2020.

1010   Kovacs, T. A. and Brune, W. H.: Total OH loss rate measurement, J. Atmos. Chem., 39(2), 105–122,
1011   doi:10.1023/A:1010614113786, 2001.

1012   Krechmer, J. E., Pagonis, D., Ziemann, P. J. and Jimenez, J. L.: Quantification of Gas-Wall Partitioning in
1013   Teflon Environmental Chambers Using Rapid Bursts of Low-Volatility Oxidized Species Generated in
1014   Situ, Environ. Sci. Technol., 50(11), 5757–5765, doi:10.1021/acs.est.6b00606, 2016.

1015   Krechmer, J. E., Day, D. A., Ziemann, P. J. and Jimenez, J. L.: Direct Measurements of Gas/Particle
1016   Partitioning and Mass Accommodation Coefficients in Environmental Chambers, Environ. Sci. Technol.,
1017   51(20), 11867–11875, doi:10.1021/acs.est.7b02144, 2017.

1018   Kwok, E. and Atkinson, R.: Estimation of hydroxyl radical reaction rate constants for gas-phase organic
1019   compounds using a structure-reactivity relationship: An update, Atmos. Environ., 29(14), 1685–1695,
1020   doi:10.1016/1352-2310(95)00069-B, 1995.

1021   Lee-Taylor, J., Hodzic, A., Madronich, S., Aumont, B., Camredon, M., and Valorso, R.: Multiday
1022   production of condensing organic aerosol mass in urban and forest outflow, Atmos. Chem. Phys., 15(2),
1023   595–615, doi:10.5194/acp-15-595-2015, 2015.

1024   Levy II, H.: Normal atmosphere: large radical and formaldehyde concentrations predicted., Science,
1025   173(3992), 141–143, doi:10.1126/science.173.3992.141, 1971.

1026   Li, R., Palm, B. B., Ortega, A. M., Hu, W., Peng, Z., Day, D. A., Knote, C., Brune, W. H., de Gouw, J. and
1027   Jimenez, J. L.: Modeling the radical chemistry in an Oxidation Flow Reactor (OFR): radical formation and
1028   recycling, sensitivities, and OH exposure estimation equation, J. Phys. Chem. A, 119(19), 4418–4432,

1029   doi:10.1021/jp509534k, 2015.

1030   Liu, X., Day, D. A., Krechmer, J. E., Brown, W., Peng, Z., Ziemann, P. J. and Jimenez, J. L.: Direct
1031   measurements of semi-volatile organic compound dynamics show near-unity mass accommodation
1032   coefficients for diverse aerosols, Commun. Chem., 2(1), 98, doi:10.1038/s42004-019-0200-x, 2019.

1033   Lu, K. D., Hofzumahaus, A., Holland, F., Bohn, B., Brauers, T., Fuchs, H., Hu, M., Häseler, R., Kita, K.,
1034   Kondo, Y., Li, X., Lou, S. R., Oebel, A., Shao, M., Zeng, L. M., Wahner, A., Zhu, T., Zhang, Y. H. and Rohrer,
1035   F.: Missing OH source in a suburban environment near Beijing: observed and modelled OH and HO 2
1036   concentrations in summer 2006, Atmos. Chem. Phys., 13(2), 1057–1080, doi:10.5194/acp-13-1057-
1037   2013, 2013.

1038   Madronich, S. and Flocke, S.: The Role of Solar Radiation in Atmospheric Chemistry, in Environmental
1039   Photochemistry. The Handbook of Environmental Chemistry (Reactions and Processes), vol 2 / 2L,
1040   edited by P. Boule, pp. 1–26, Springer, Berlin, Heidelberg., 1999.

1041   Mao, J., Ren, X., Brune, W. H., Olson, J. R., Crawford, J. H., Fried, a., Huey, L. G., Cohen, R. C., Heikes,
1042   B., Singh, H. B., Blake, D. R., Sachse, G. W., Diskin, G. S., Hall, S. R. and Shetter, R. E.: Airborne
1043   measurement of OH reactivity during INTEX-B, Atmos. Chem. Phys., 9(1), 163–173, doi:10.5194/acp-9-
1044   163-2009, 2009.

1045   Matsunaga, A. and Ziemann, P. J.: Gas-Wall Partitioning of Organic Compounds in a Teflon Film
1046   Chamber and Potential Effects on Reaction Product and Aerosol Yield Measurements, Aerosol Sci.
1047   Technol., 44(10), 881–892, doi:10.1080/02786826.2010.501044, 2010.

1048   Mouchel-Vallon, C., Lee-Taylor, J., Hodzic, A., Artaxo, P., Aumont, B., Camredon, M., Gurarie, D.,
1049   Jimenez, J.-L., Lenschow, D. H., Martin, S. T., Nascimento, J., Orlando, J. J., Palm, B. B., Shilling, J. E.,
1050   Shrivastava, M. and Madronich, S.: Exploration of oxidative chemistry and secondary organic aerosol
1051   formation in the Amazon during the wet season: explicit modeling of the Manaus urban plume with
1052   GECKO-A, Atmos. Chem. Phys., 20(10), 5995–6014, doi:10.5194/acp-20-5995-2020, 2020.

1053   Nakashima, Y., Tsurumaru, H., Imamura, T., Bejan, I., Wenger, J. C. and Kajii, Y.: Total OH reactivity
1054   measurements in laboratory studies of the photooxidation of isoprene, Atmos. Environ., 62, 243–247,
1055   doi:10.1016/j.atmosenv.2012.08.033, 2012.

1056   Nannoolal, Y., Rarey, J. and Ramjugernath, D.: Estimation of pure component properties part 3.
1057   Estimation of the vapor pressure of non-electrolyte organic compounds via group contribution and
1058   group interactions, Fluid Phase Equilib., 269, 117–133, doi:10.1016/j.fluid.2008.04.020, 2008.

1059   Nehr, S., Bohn, B., Fuchs, H., Häseler, R., Hofzumahaus, A., Li, X., Rohrer, F., Tillmann, R. and Wahner,
1060   A.: Atmospheric photochemistry of aromatic hydrocarbons: OH budgets during SAPHIR chamber
1061   experiments, Atmos. Chem. Phys., 14(13), 6941–6952, doi:10.5194/acp-14-6941-2014, 2014.

1062   Nel, A.: Air Pollution-Related Illness: Effects of Particles, Science (80-.)., 308(5723), 804–806,
1063   doi:10.1126/science.1108752, 2005.

1064   Nguyen, T. B., Crounse, J. D., Schwantes, R. H., Teng, A. P., Bates, K. H., Zhang, X., St. Clair, J. M., Brune,
1065   W. H., Tyndall, G. S., Keutsch, F. N., Seinfeld, J. H., and Wennberg, P. O.: Overview of the Focused
1066   Isoprene eXperiment at the California Institute of Technology (FIXCIT): mechanistic chamber studies on
1067   the oxidation of biogenic compounds, Atmos. Chem. Phys., 14, 13531–13549, 2014.

1068   Nölscher, A. C., Butler, T., Auld, J., Veres, P., Muñoz, A., Taraborrelli, D., Vereecken, L., Lelieveld, J. and
1069   Williams, J.: Using total OH reactivity to assess isoprene photooxidation via measurement and model,
1070   Atmos. Environ., 89, 453–463, doi:10.1016/j.atmosenv.2014.02.024, 2014.

1071   Nölscher, A. C., Yañez-Serrano, A. M., Wolff, S., de Araujo, A. C., Lavrič, J. V., Kesselmeier, J. and
1072   Williams, J.: Unexpected seasonality in quantity and composition of Amazon rainforest air reactivity,
1073   Nat. Commun., 7, 10383, doi:10.1038/ncomms10383, 2016.

1074   Novelli, A., Kaminski, M., Rolletter, M., Acir, I. H., Bohn, B., Dorn, H. P., Li, X., Lutz, A., Nehr, S., Rohrer,
1075   F., Tillmann, R., Wegener, R., Holland, F., Hofzumahaus, A., Kiendler-Scharr, A., Wahner, A., and Fuchs,
1076   H.: Evaluation of OH and HO2 concentrations and their budgets during photooxidation of 2-methyl-3-
1077   butene-2-ol (MBO) in the atmospheric simulation chamber SAPHIR, Atmos. Chem. Phys., 18, 11409-
1078   11422, doi:10.5194/acp-18-11409-2018, 2018.

1079   Orlando, J. J. and Tyndall, G. S.: Laboratory studies of organic peroxy radical chemistry: an overview

with emphasis on recent issues of atmospheric significance, Chem. Soc. Rev., 41(19), 6294–6317, doi:10.1039/c2cs35166h, 2012.

Pankow, J. F. and Asher, W. E.: SIMPOL.1: A simple group contribution method for predicting vapor pressures and enthalpies of vaporization of multifunctional organic compounds, Atmos. Chem. Phys., 8(10), 2773–2796, doi:10.5194/acp-8-2773-2008, 2008.

Peng, Z. and Jimenez, J. L.: Modeling of the chemistry in oxidation flow reactors with high initial NO, Atmos. Chem. Phys., 17(19), 11991–12010, doi:10.5194/acp-17-11991-2017, 2017.

Peng, Z. and Jimenez, J. L.: KinSim: A Research-Grade, User-Friendly, Visual Kinetics Simulator for Chemical-Kinetics and Environmental-Chemistry Teaching, J. Chem. Educ., 96(4), 806–811, doi:10.1021/acs.jchemed.9b00033, 2019.

Peng, Z. and Jimenez, J. L.: Radical chemistry in oxidation flow reactors for atmospheric chemistry research, Chem. Soc. Rev., doi:10.1039/C9CS00766K, 2020.

Peng, Z., Day, D. A., Stark, H., Li, R., Lee-Taylor, J., Palm, B. B., Brune, W. H. and Jimenez, J. L.: HOx radical chemistry in oxidation flow reactors with low-pressure mercury lamps systematically examined by modeling, Atmos. Meas. Tech., 8(11), 4863–4890, doi:10.5194/amt-8-4863-2015, 2015.

Peng, Z., Day, D. A., Ortega, A. M., Palm, B. B., Hu, W., Stark, H., Li, R., Tsigaridis, K., Brune, W. H. and Jimenez, J. L.: Non-OH chemistry in oxidation flow reactors for the study of atmospheric chemistry systematically examined by modeling, Atmos. Chem. Phys., 16(7), 4283–4305, doi:10.5194/acp-16-4283-2016, 2016.

Peng, Z., Palm, B. B., Day, D. A., Talukdar, R. K., Hu, W., Lambe, A. T., Brune, W. H. and Jimenez, J. L.: Model Evaluation of New Techniques for Maintaining High-NO Conditions in Oxidation Flow Reactors for the Study of OH-Initiated Atmospheric Chemistry, ACS Earth Sp. Chem., 2(2), 72–86, doi:10.1021/acsearthspacechem.7b00070, 2018.

Peng, Z., Lee-Taylor, J., Orlando, J. J., Tyndall, G. S. and Jimenez, J. L.: Organic peroxy radical chemistry in oxidation flow reactors and environmental chambers and their atmospheric relevance, Atmos. Chem. Phys., 19(2), 813–834, doi:10.5194/acp-19-813-2019, 2019.

Rohrer, F., Bohn, B., Brauers, T., Brüning, D., Johnen, F.-J., Wahner, A., and Kleffmann, J.: Characterisation of the photolytic HONO-source in the atmosphere simulation chamber SAPHIR, https://doi.org/10.5194/acp-5-2189-2005, 2005.

Sato, K., Nakashima, Y., Morino, Y., Imamura, T., Kurokawa, J. and Kajii, Y.: Total OH reactivity measurements for the OH-initiated oxidation of aromatic hydrocarbons in the presence of NO x, Atmos. Environ., 171, 272–278, doi:10.1016/j.atmosenv.2017.10.036, 2017.

Schwantes, R. H., Schilling, K. A., McVay, R. C., Lignell, H., Coggon, M. M., Zhang, X., Wennberg, P. O. and Seinfeld, J. H.: Formation of highly oxygenated low-volatility products from cresol oxidation, Atmos. Chem. Phys., 17(5), 3453–3474, doi:10.5194/acp-17-3453-2017, 2017.

Siese, M., Becker, K. H., Brockmann, K. J., Geiger, H., Hofzumahaus, A., Holland, F., Mihelcic, D., and Wirtz, K.: Direct measurement of OH radicals from ozonolysis of selected alkenes: a EUPHORE simulation chamber study, Environ. Sci. Technol., 35, 4660–4667, 2001.

Stocker, T. F., Qin, D., Plattner, G.-K., Tignor, M., Allen, S. K., Boschung, J., Nauels, A., Xia, Y., Bex, V. and Midgley, P. M.: Climate Change 2013 - The Physical Science Basis, edited by Intergovernmental Panel on Climate Change, Cambridge University Press, Cambridge., 2014.

Stone, D., Whalley, L. K. and Heard, D. E.: Tropospheric OH and HO2 radicals: field measurements and model comparisons, Chem. Soc. Rev., 41(19), 6348, doi:10.1039/c2cs35140d, 2012.

Turro, N. J., Ramamurthy, V. and Scaiano, J. C.: Principles of Molecular Photochemistry: An Introduction, University Science Books, Sausalito, CA, USA. [online] Available from: http://www.uscibooks.com/turro2.htm, 2009.

US EPA: Estimation Programs Interface SuiteTM, 2012.

Valorso, R., Aumont, B., Camredon, M., Raventos-Duran, T., Mouchel-Vallon, C., Ng, N. L., Seinfeld, J. H., Lee-Taylor, J. and Madronich, S.: Explicit modelling of SOA formation from α-pinene photooxidation: sensitivity to vapour pressure estimation, Atmos. Chem. Phys., 11(14), 6895–6910, doi:10.5194/acp-

1130   11-6895-2011, 2011.

1131   Verwer, J. G.: Gauss–Seidel Iteration for Stiff ODES from Chemical Kinetics, SIAM J. Sci. Comput., 15(5),
1132   1243–1250, doi:10.1137/0915076, 1994.

1133   Verwer, J. G., Blom, J. G., van Loon, M. and Spee, E. J.: A comparison of stiff ODE solvers for atmospheric
1134   chemistry problems, Atmos. Environ., 30(1), 49–58, doi:10.1016/1352-2310(95)00283-5, 1996.

1135   Wennberg, P. O., Bates, K. H., Crounse, J. D., Dodson, L. G., McVay, R. C., Mertens, L. A., Nguyen, T. B.,
1136   Praske, E., Schwantes, R. H., Smarte, M. D., St Clair, J. M., Teng, A. P., Zhang, X. and Seinfeld, J. H.: Gas-
1137   Phase Reactions of Isoprene and Its Major Oxidation Products, Chem. Rev., 118(7), 3337–3390,
1138   doi:10.1021/acs.chemrev.7b00439, 2018.

1139   Whalley, L. K., Stone, D., Bandy, B., Dunmore, R., Hamilton, J. F., Hopkins, J., Lee, J. D., Lewis, A. C. and
1140   Heard, D. E.: Atmospheric OH reactivity in central London: observations, model predictions and
1141   estimates of in situ ozone production, Atmos. Chem. Phys., 16(4), 2109–2122, doi:10.5194/acp-16-
1142   2109-2016, 2016.

1143   Williams, J. and Brune, W.: A roadmap for OH reactivity research, Atmos. Environ., 106, 371–372,
1144   doi:10.1016/j.atmosenv.2015.02.017, 2015.

1145   Wofsy, S. C., Apel, E., Blake, D. R., Brock, C. A., Brune, W. H., Bui, T. P., Daube, B. C., Dibb, J. E., Diskin,
1146   G. S., Elkiins, J. W., Froyd, K., Hall, S. R., Hanisco, T. F., Huey, L. G., Jimenez, J. L., McKain, K., Montzka,
1147   S. A., Ryerson, T. B., Schwarz, J. P., Stephens, B. B., Weinzierl, B. and Wennberg, P.: ATom: Merged
1148   Atmospheric Chemistry, Trace Gases, and Aerosols, Oak Ridge, Tennessee, USA., 2021.

1149   Yang, Y., Shao, M., Wang, X., Nölscher, A. C., Kessel, S., Guenther, A. and Williams, J.: Towards a
1150   quantitative understanding of total OH reactivity: A review, Atmos. Environ., 134(2), 147–161,
1151   doi:10.1016/j.atmosenv.2016.03.010, 2016.

1152   Zannoni, N., Gros, V., Lanza, M., Sarda, R., Bonsang, B., Kalogridis, C., Preunkert, S., Legrand, M.,
1153   Jambert, C., Boissard, C. and Lathiere, J.: OH reactivity and concentrations of biogenic volatile organic
1154   compounds in a Mediterranean forest of downy oak trees, Atmos. Chem. Phys., 16(3), 1619–1636,
1155   doi:10.5194/acp-16-1619-2016, 2016.

1156   Ziemann, P. J. and Atkinson, R.: Kinetics, products, and mechanisms of secondary organic aerosol
1157   formation, Chem. Soc. Rev., 41(19), 6582–6605, doi:10.1039/c2cs35122f, 2012.
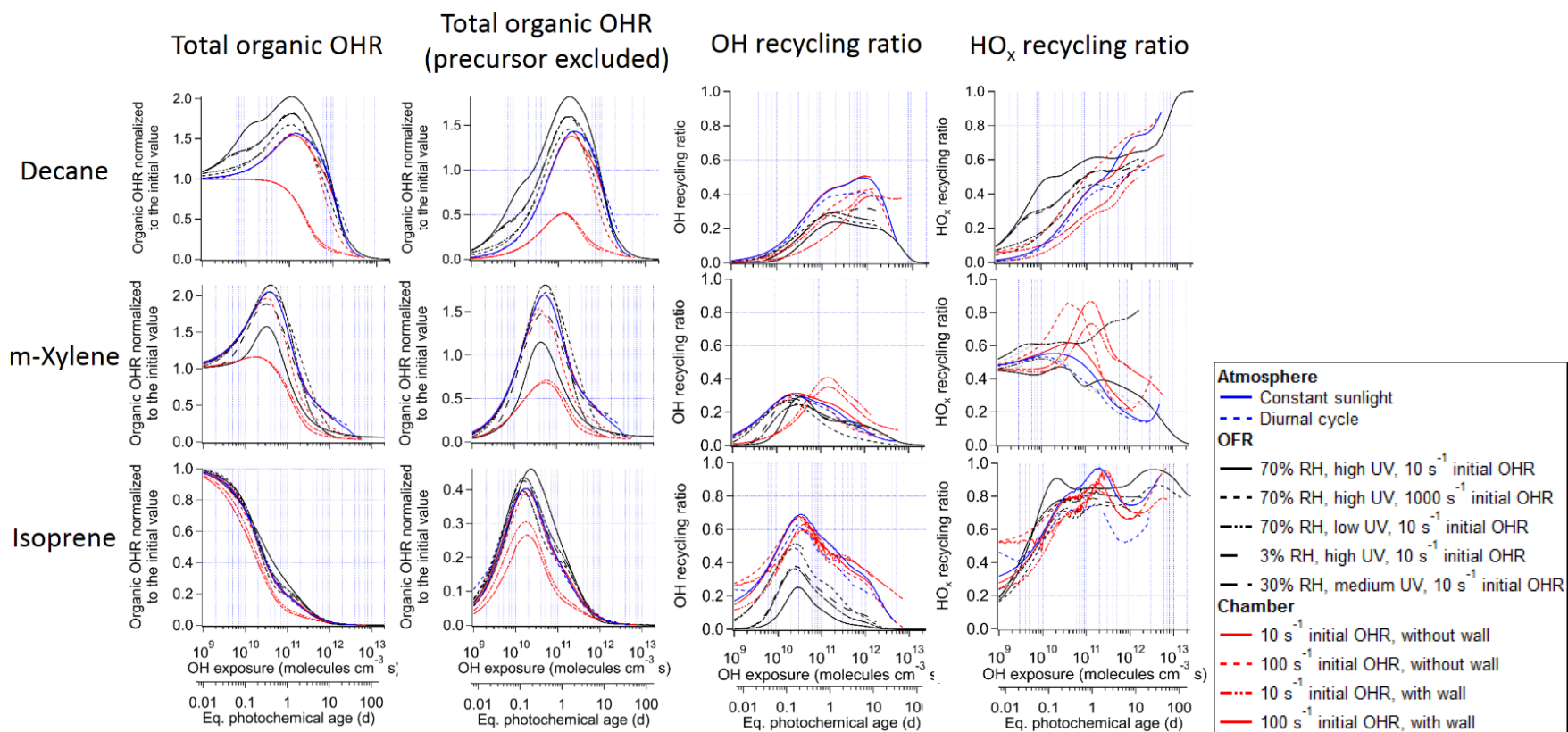
Figure 1. Total organic OH reactivity (OHR) with and without the contribution of the precursor, OH recycling ratio (β_1), and HO_x recycling ratio (β_2) as a function of OH exposure (or equivalent photochemical age; second x-axis) in the photooxidations of decane, isoprene, and m-xylene under different conditions in the atmosphere, oxidation flow reactor (OFR), and chamber.
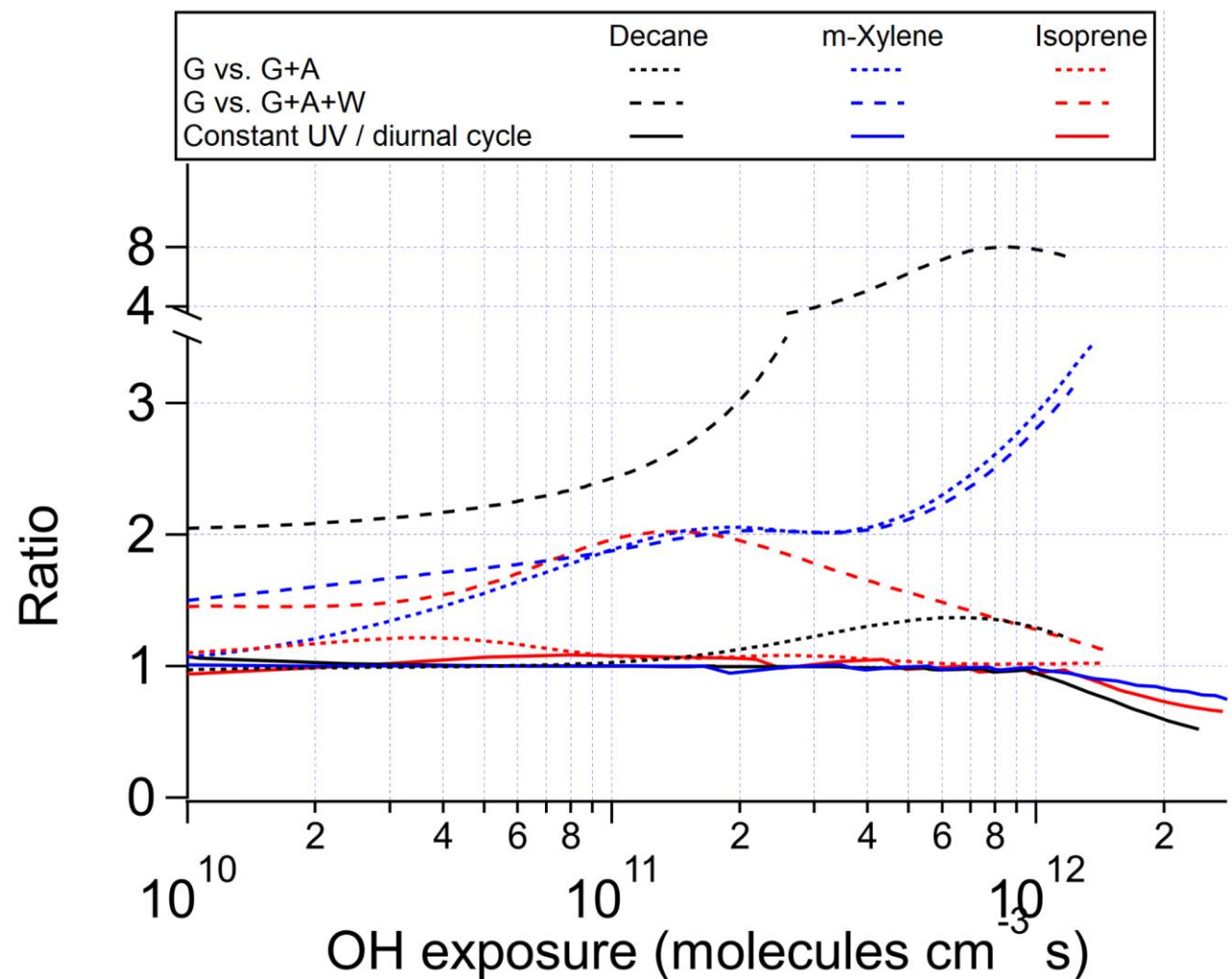
Figure 2. Ratios of OHR of the products present in the gas phase between the chamber cases without gas-particle-wall partitioning and i) with gas-particle (G vs. G+A) or ii) gas-particle-wall partitioning (G vs. G+A+W) at initial OHR of 10 and 100 s⁻¹, and between the ambient cases with constant and diurnal sunlight for the photooxidations of decane, m-xylene, and isoprene as a function of OH exposure.
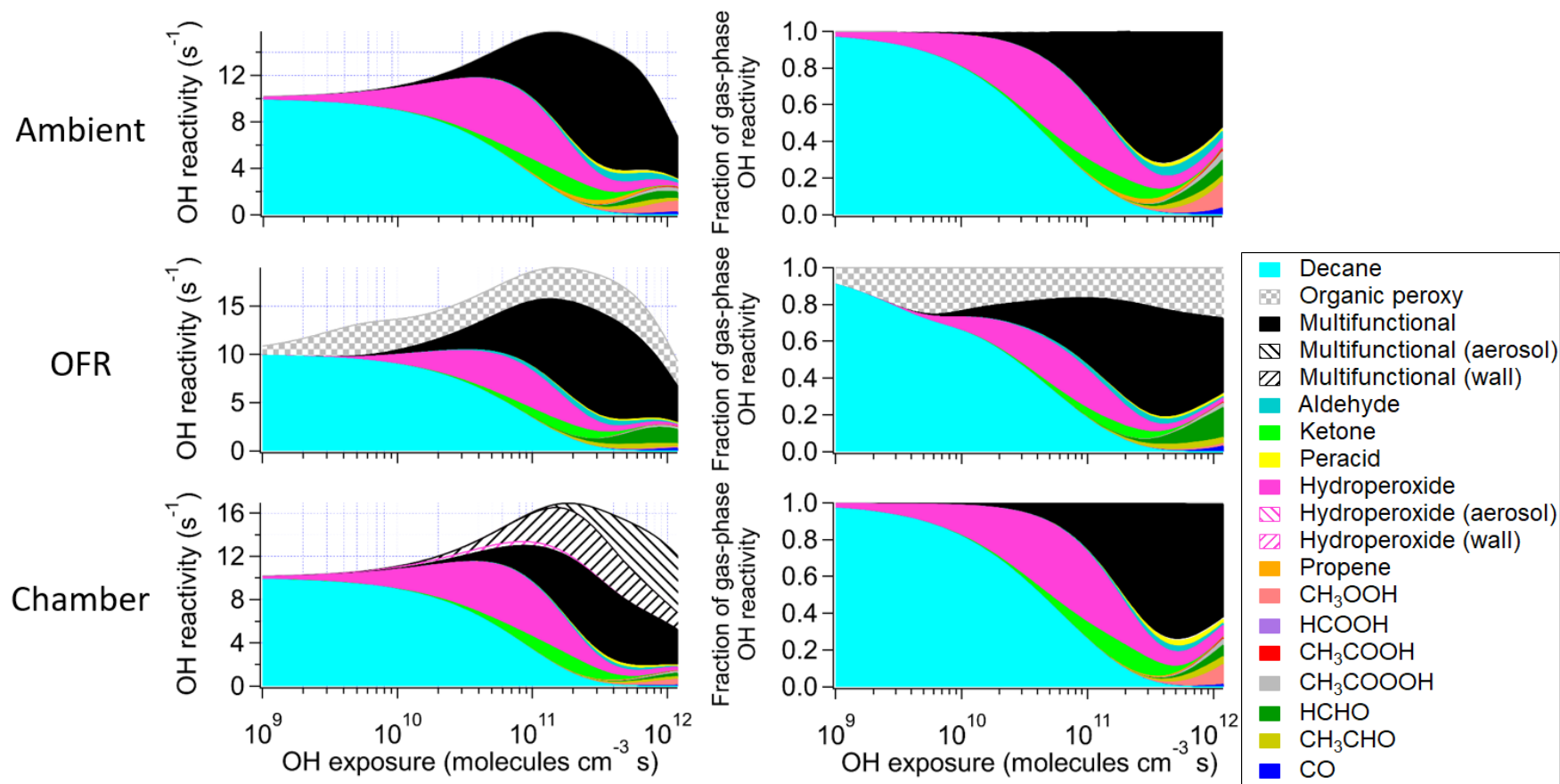
Figure 3. Absolute and fractional contributions to the organic OHR during decane photooxidation of the main species and types of species as a function of OH exposure in the ambient case with constant sunlight; the OFR case with relative humidity of 30%, medium UV lamp setting, and initial OHR of 10 s^{-1}; and the chamber case with initial OHR of 10 s^{-1} and gas-wall partitioning. The types of species shown in this figure exclude the C1 and C2 species listed separately. The OHR of the particle- and wall-phase species are the values as if those species are gas-phase OHR contributors, although they actually do not react with OH in the simulations.
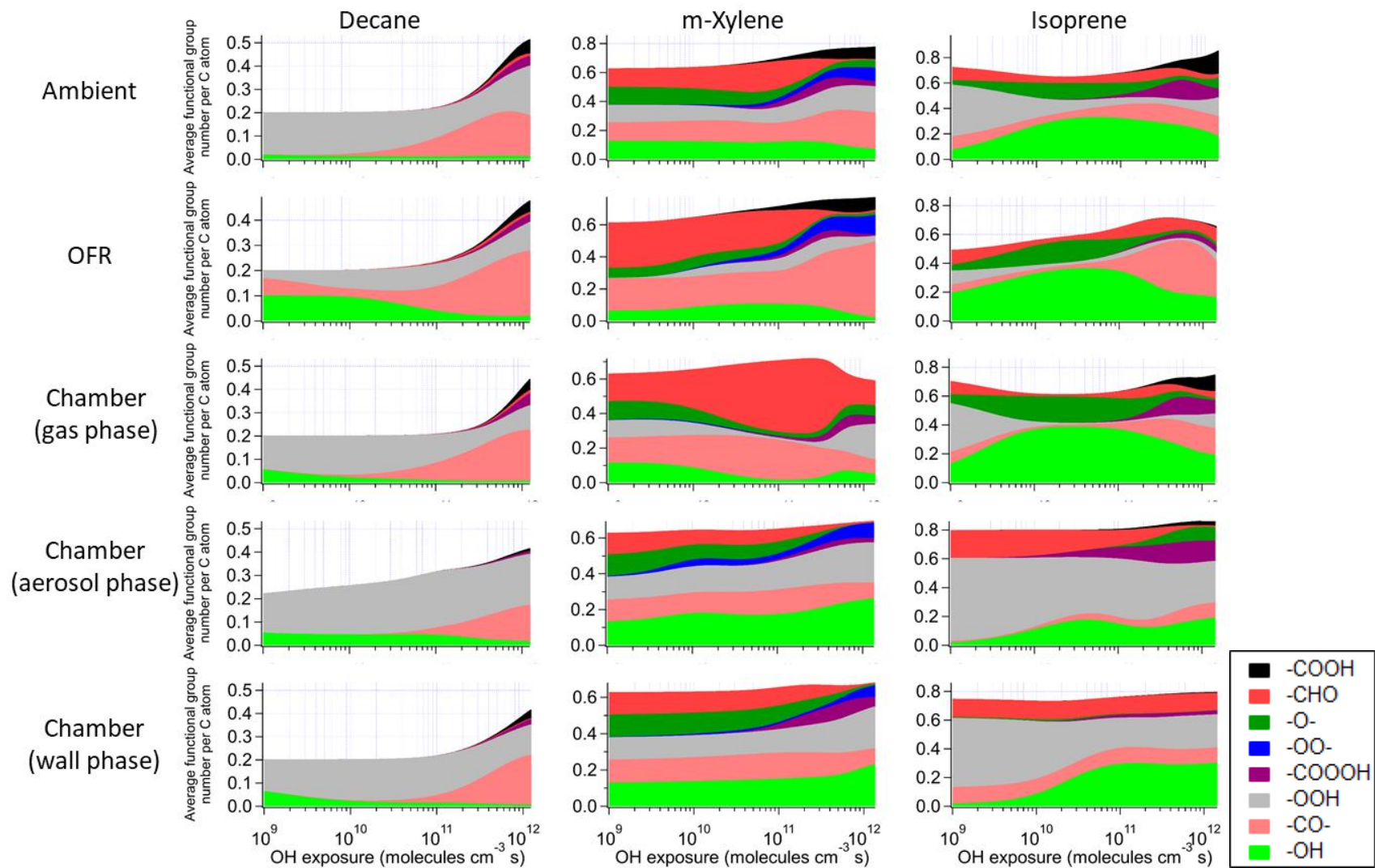
Figure 4. Average number of functional group per C atom as a function of OH exposure in the saturated multifunctional species in the ambient case with constant sunlight, the OFR case with relative humidity of 70%, high UV lamp setting, and initial OHR of 10 s⁻¹, and the gas and wall phases in the chamber case with initial OHR of 10 s⁻¹ and gas-wall partitioning of the photooxidations of decane, m-xylene, and isoprene. Note that the functional group " O " represents ether, ester,

~~and epoxy groups in the GECKO-A model.~~**Figure 4.** Average number of functional group per C atom as a function of OH exposure in the saturated multifunctional species in the ambient case with constant sunlight, the OFR case with relative humidity of 70%, high UV lamp setting, and initial OHR of 10 s^{-1}, and the gas, aerosol, and wall phases in the chamber case with initial OHR of 10 s-1 and gas-particle-wall partitioning of the photooxidations of decane, m-xylene, and isoprene. Note that the functional group "-O-" represents ether, ester, and epoxy groups in the GECKO-A model.
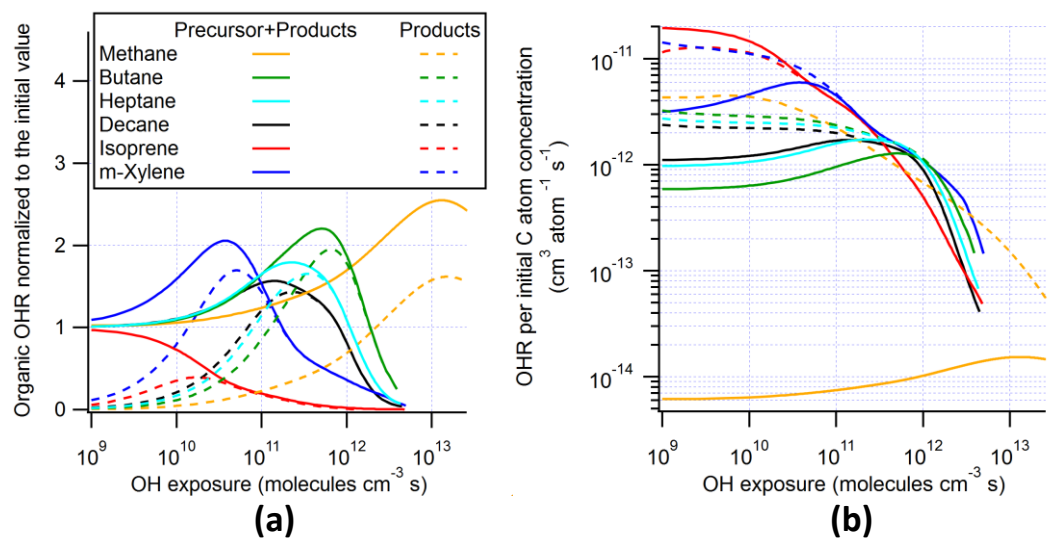
Figure 5. (a) OHR and (b) OHR per initial C atom concentration of the organics (including and excluding the precursor) as a function of OH exposure in the ambient cases with constant sunlight of the photooxidation of methane, butane, heptane, decane, isoprene, and m-xylene.
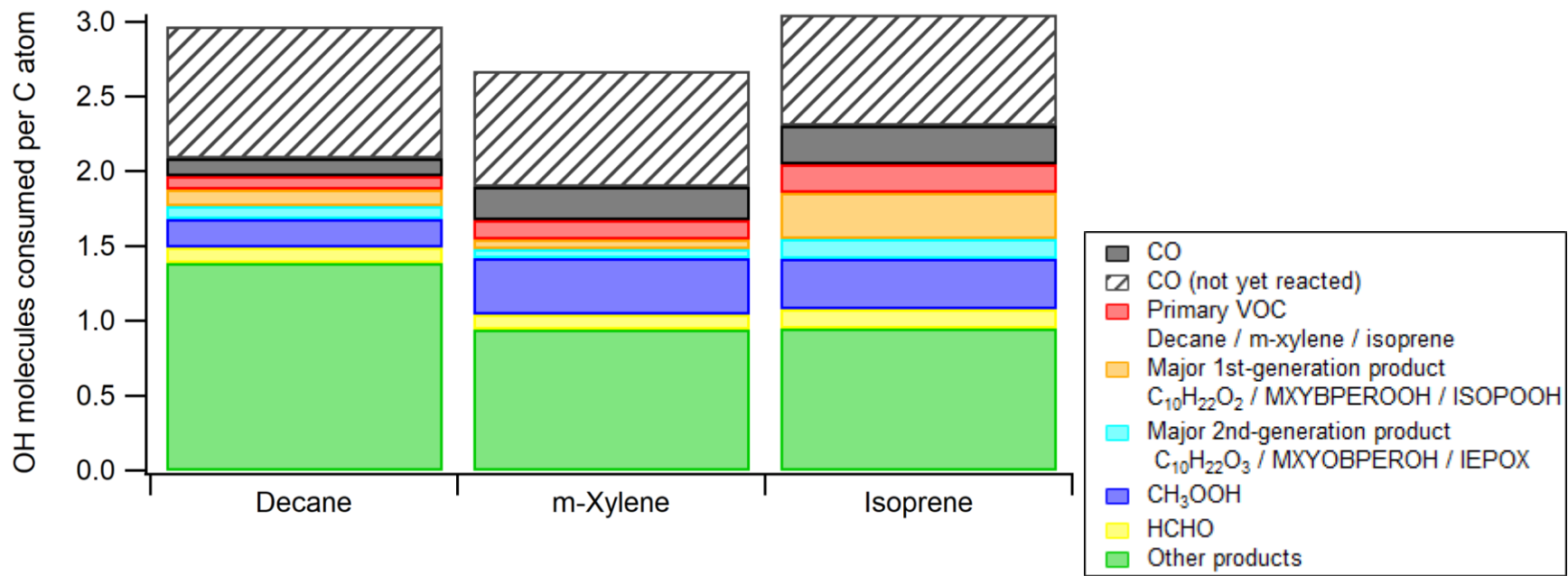
Figure 6. Average numbers of OH molecules consumed per C atom in the ambient cases with constant sunlight during photooxidation of isoprene, decane, and m-xylene. The contribution from CO that is not yet oxidized by OH at the end of simulation is also added to ensure that each CO molecule consumed one OH radical. ISOPOOH, IEPOX, $C_{10}H_{22}O_2$, $C_{10}H_{22}O_3$, $C_8H_{10}O_2$, and $C_8H_{10}O_3$ are isoprene hydroxyl hydroperoxides, isoprene epoxydiols, decyl hydroperoxides, hydroxydecyl hydroperoxides, m-xylenyl hydroperoxide, and hydroperoxy m-xylenol, respectively. Figure 6. Average numbers of OH molecules consumed per C atom in the ambient cases with constant sunlight during photooxidation of isoprene, decane, and m-xylene. The contribution from CO that is not yet oxidized by OH at the end of simulation is also added to ensure that each CO molecule consumed one OH radical. ISOPOOH, IEPOX, $C_{10}H_{22}O_2$, and $C_{10}H_{22}O_3$ are isoprene hydroxyl hydroperoxides, isoprene epoxydiols, decyl hydroperoxides, and hydroxydecyl hydroperoxides, respectively. See Scheme S1 for the structures of MXYBPEROOH and MXYOBPEROH.

Table 1. Conditions and integration timesteps of the simulations in the present work.

Precursor	Environment	Relative humidity (%)	UV	Initial OH reactivity (s⁻¹)	Integration timestep (s)
Methane	Ambient	30	Constant sunlight[a]	10	KinSim-determined[b]
	Oxidation flow reactor	70	High lamp setting[c]		
Decane	Ambient	30	Constant sunlight[a]	10	Min: 0.1; Max: 120 (1 d), 300 (2–10 d)
			Diurnal sunlight		
	Oxidation flow reactor	70	High lamp setting[c]	10	0.0025
		70	Low lamp setting[e]	10	
		30	Medium lamp setting[f]	10	
		3	High lamp setting[c]	10	
		70	High lamp setting[c]	1000	
	Chamber (gas-phase only)	30	CU Chamber spectrum[g]	10	Min: 0.1; Max: 120 (6 d), 300 (7–30 d if needed)
				100	
	Chamber (gas-particle partitioning)			10	
				100	
	Chamber (gas-particle -wall partitioning)			10	
				100	
m-Xylene	Ambient	30	Constant sunlight[a]	10	Min: 0.1; Max: 120 (1 d), 300 (2–10 d)
			Diurnal sunlight[c]		
	Oxidation flow reactor	70	High lamp setting[c]	10	0.0025
		70	Low lamp setting[e]	10	
		30	Medium lamp setting[f]	10	
		3	High lamp setting[c]	10	
		70	High lamp setting[c]	1000	
	Chamber (gas-phase only)	30	CU Chamber spectrum[g]	10	Min: 0.1; Max: 120 (6 d), 300 (7–30 d if needed)
				100	
	Chamber (gas-particle partitioning)			10	
				100	
	Chamber (gas-particle -wall partitioning)			10	
				100	
Isoprene	Ambient	30	Constant sunlight[a]	10	Min: 0.1; Max: 10 (1 d), 120 (2–10 d)
			Diurnal sunlight[c]		
	Oxidation flow reactor	70	High lamp setting[c]	10	0.001
		70	Low lamp setting[e]	10	
		30	Medium lamp setting[f]	10	
		3	High lamp setting[c]	10	
		70	High lamp setting[c]	1000	
		30	Medium lamp setting[f] + 5x CU Chamber spectrum[g]	10	

		30	Medium lamp setting[f] + 10000x CU Chamber spectrum[g]	10	
	Chamber (gas-phase only)	30	CU Chamber spectrum[g]	10	Min: 0.1; Max: 10 (6 d), 120 (7–30 d if needed)
				100	
	Chamber (gas-particle partitioning)			10	
				100	
	Chamber (gas-particle -wall partitioning)			10	
				100	
Butane	Ambient	30	Constant sunlight[a]	10	Min: 0.1; Max: 120 (1 d), 300 (2–10 d)
Heptane	Ambient	30	Constant sunlight[a]	10	Min: 0.1; Max: 120 (1 d), 300 (2–10 d)

[a] At solar zenith angle of 45°.

[b] Simulation performed in the solver KinSim, which fully controls its integration timestep selection.

[c] Diurnal variation between solar zenith angles of 0 and 90°.

[d] UV at 185 nm = 1×10^{14} photons cm^{-2} s^{-1}; UV at 254 nm = 8.5×10^{15} photons cm^{-2} s^{-1}.

[e] UV at 185 nm = 1×10^{11} photons cm^{-2} s^{-1}; UV at 254 nm = 4.2×10^{13} photons cm^{-2} s^{-1}.

[f] UV at 185 nm = 1×10^{13} photons cm^{-2} s^{-1}; UV at 254 nm = 1.4×10^{15} photons cm^{-2} s^{-1}.

[g] UV source spectrum of the University of Colorado Environmental Chamber Facility (Krechmer et al., 2017).